AD-A283 462



①

*ARMY RESEARCH LABORATORY*

**AR**

# Target Recognition in Ultra-Wideband SAR Imagery

by Vincent Sabio

ARL-TR-378

August 1994

DTIC
ELECTE
AUG 19, 1994
S B D

94-26388

94 8 18 199   DTIC QUALITY INSPECTED 1

# REPORT DOCUMENTATION PAGE

Public reporting burden for this collection of information is estimated to average 1 hour per response, including the time for reviewing instructions, searching existing data sources, gathering and maintaining the data needed, and completing and reviewing the collection of information. Send comments regarding this burden estimate or any other aspect of this collection of information, including suggestions for reducing the burden, to Washington Headquarters Services, Directorate for Information Operations and Reports, 1215 Jefferson Davis Highway, Suite 1204, Arlington, VA 22202-4302, and to the Office of Management and Budget, Paperwork Reduction Project (0704-0188), Washington, DC 20503

| 1. AGENCY USE ONLY (Leave blank) | 2. REPORT DATE <br> August 1994 | 3. REPORT TYPE AND DATES COVERED <br> Final, from January 1993 to July 1993 |
|---|---|---|

| 4. TITLE AND SUBTITLE <br> Target Recognition in Ultra-Wideband SAR Imagery | 5. FUNDING NUMBERS <br> PE: 61102AH44 |
|---|---|
| 6. AUTHOR(S) <br> Vincent Sabio | |

| 7. PERFORMING ORGANIZATION NAME(S) AND ADDRESS(ES) <br> U.S. Army Research Laboratory <br> Attn: AMSRL-SS-SG <br> 2800 Powder Mill Road <br> Adelphi, MD 20783-1197 | 8. PERFORMING ORGANIZATION REPORT NUMBER <br> ARL-TR-378 |
|---|---|

| 9. SPONSORING/MONITORING AGENCY NAME(S) AND ADDRESS(ES) <br> U.S. Army Research Laboratory <br> 2800 Powder Mill Road <br> Adelphi, MD 20783-1197 | 10. SPONSORING/MONITORING AGENCY REPORT NUMBER |
|---|---|

**11. SUPPLEMENTARY NOTES**

AMS code: 611102.H44
ARL project: 3AE153

| 12a. DISTRIBUTION/AVAILABILITY STATEMENT <br><br> Approved for public release; distribution unlimited. | 12b. DISTRIBUTION CODE |
|---|---|

**13. ABSTRACT** (Maximum 200 words)

Ultra-wideband (UWB) synthetic-aperture radar (SAR) images—with greater than 95-percent bandwidth occupancy—provide the potential for recognition of targets embedded in foliage; recognition methods in these applications are based on wideband resonant signatures of the targets. Currently, resonance-extraction techniques hinge on contemporary adaptations of Prony's method; this method, however, has poor performance in the presence of noise and is very computationally intensive. A form of resonance analysis is proposed that applies linear-transform methods. Both the Fourier basis and two multiresolution bases—the Haar wavelet and the Gaussian basis—were employed in the analysis. Target-declaration confidences were established by simple correlation of the two sets of spectral coefficients—one set from the transformed data, and the other from a synthetic template generated from both prediction and empirical observation. This permits a fast, efficient scheme for recognition of target resonance effects in wideband imagery. Five UWB images from the Army Research Laboratory's UWB SAR instrumentation system were analyzed through the use of canonical targets (dipoles) of differing dimension and orientation. Results are presented and summarized for each of the targets and transform methods employed in the analysis.

| 14. SUBJECT TERMS <br> Ultra-wideband, synthetic aperture radar, SAR, automatic target recognition, ATR | 15. NUMBER OF PAGES <br> 94 |
|---|---|
| | 16. PRICE CODE |

| 17. SECURITY CLASSIFICATION OF REPORT <br> Unclassified | 18. SECURITY CLASSIFICATION OF THIS PAGE <br> Unclassified | 19. SECURITY CLASSIFICATION OF ABSTRACT <br> Unclassified | 20. LIMITATION OF ABSTRACT <br> UL |
|---|---|---|---|

# Contents

# Appendices

# Figures

# Tables

6

# 1. Introduction

## 1.1 Motivation

The ability to "see" through foliage has long been a subject of investigation for both civilian applications (finding downed aircraft in dense forestation) and military requirements (finding tactical targets concealed in foliage).

Wideband radars operating in the low microwave bands (and below) provide the potential for automatic recognition of foliage-concealed objects by spectral analysis of the objects' signatures. These spectral signatures appear to lend themselves to analysis by multiresolution methods—such as the wavelet transform—instead of classical Fourier methods. It is the purpose of this report to show that multiresolution methods do indeed provide target-recognition performance superior to the Fourier transform in terms of target-detection reliability, clutter rejection, and computational efficiency.

## 1.2 Organization

I begin by presenting the motivation for synthetic-aperture radar (SAR) and briefly describing the ultra-wideband foliage-penetrating SAR designed by the Army Research Laboratory (ARL) in Adelphi, MD. An analysis of wideband target signatures is presented, with a focus on target resonance effects and modeling. Resonance-based target-recognition methods are introduced, and analyses through multiresolution techniques are motivated. Performance of various multiresolution bases is presented and compared to Fourier-basis performance. Finally, conclusions are provided, with recommendations for further investigation. Appendix A discusses SAR image formation, including conventional Fourier processing and the back-projection algorithm. Appendix B tabulates the spectral data used in the analysis, and appendix C summarizes the performance data.

## 1.3 Contributions to the State of the Art

Currently, the preferred method for spectral analysis of resonant signatures—the singularity expansion method (SEM), a contemporary adaptation of Prony's algorithm [1]—is computationally intensive and requires unrealistic signal-to-noise levels [2]. An alternative approach is to use a Fourier transform to recover the harmonic components present in the resonant signature, but Fourier methods do not accurately model the frequency-dependent decay characteristics

of the response. Instead, I present a method of resonant-signature analysis using multiresolution bases (e.g., the wavelet transform), which model the behavior of wideband resonant decays better than Fourier methods, with lower computational order and greater noise immunity than the Prony method. Although I use Fourier performance as a basis for comparison with multiresolution methods, I do not use Prony's algorithm because of its poor performance in low signal-to-noise environments [3].

# 2. Background and Motivations

## 2.1 Motivation for Ultra-Wideband SAR

Range resolution in real-aperture radar systems is generally defined in terms of system bandwidth ($\Delta f$) and propagation velocity ($c$) [4],

$$\delta_{Range} = \frac{c}{2\Delta f} \, , \tag{1}$$

while azimuth and elevation resolutions are defined by operating wavelength ($\lambda$), aperture dimension in the orientation of interest ($L_A$), and range to target ($R$) [5],

$$\delta_{Az/El} = \frac{\lambda R}{L_A} \, . \tag{2}$$

Automated target-recognition systems generally require a large number of resolution cells ("pixels") on the target to achieve a specific performance level [6], and human-based targeting systems have similar requirements. Thus, the desire for automatic target recognition (ATR) capabilities has motivated increases in system bandwidths, operating frequencies, and aperture sizes. Increased system bandwidth is often accommodated by the use of higher carrier frequencies, so that bandwidth occupancy is kept relatively small ("narrowband") and system complexity low; these higher carrier frequencies have the additional benefit of increased azimuth resolution.

Higher frequencies, however, suffer from increased scattering and atmospheric attenuation. Attenuation effects at higher frequencies—from scattering and ohmic loss of the foliage medium—preclude penetration into foliage, thwarting attempts to locate targets obscured by trees or other flora. Thus, foliage-penetrating radars are forced into lower frequency bands (generally L-band and below), where the large bandwidths required for high range resolution yield high bandwidth occupancies—sometimes several octaves or more. Lower operating frequencies also yield poorer azimuth resolution, which can be a serious problem for target-recognition tasks that require fine resolution in both range and azimuth. Fixing the operating frequency of the radar, we can improve azimuth resolution by decreasing the range to the target or increasing the aperture size in the azimuth dimension. Since target range is usually dictated by operational constraints—and thus not subject to alteration—aperture modification remains the only option for improving azimuth resolution.

In the real-aperture case, however, it is not practical to achieve high resolution by simply increasing the physical aperture; for example, at $\lambda = 1$ ft and $R = 1000$ ft (short range in most applications), a 1000-ft antenna would be required to achieve an azimuth resolution of 1 ft. Aperture sizes such as these are often impractical at fixed sites, and entirely unreasonable in mobile applications. Thus, the ability to synthesize a large aperture by modeling it as a coherent, linear array of smaller antennas is critical to achieving reasonably high azimuth resolutions at low operating frequencies. The marriage of synthetic-aperture concepts and high system bandwidths holds the promise of high-resolution imaging radars at the low operating bands required for foliage penetration.

## 2.2 UWB FOPEN SAR

### 2.2.1 Radar Description

ARL has designed and constructed a fully polarimetric ultra-wideband (UWB) foliage-penetrating (FOPEN) SAR for the purpose of exploring the capability to locate and recognize targets embedded in foliage; the program is being executed in collaboration with the Air Force Wright Laboratories, the Advanced Research Projects Agency, the Houston Area Research Center, the Boeing Aircraft Company, Ohio State University, and the University of Maryland.

The radar is an instrumentation system that traverses a 104-m laser-leveled track on the roof of a four-story building within the ARL compound; about 80 hours (10 days of good weather) are required for collecting one complete aperture of data. The target area extends from 112 to 267 m in range, mostly populated by deciduous trees and smaller flora. The tree line begins at a slant range of approximately 160 m from the rooftop aperture. Figure 1 is a schematic of the radar/data-collection orientation and image area. The letters A through G in the figure denote target locations in the images processed (sect. 3.2.1); X denotes the location of a corner reflector that is used as a basis for calibration among images.

The UWB system is considered to be ultra-wideband because of its high bandwidth occupancy. If *relative bandwidth* is defined as the ratio of bandwidth to center frequency,

$$Q = \frac{\Delta f}{f} = \frac{\Delta f}{(f_{hi} + f_{lo})/2} , \tag{3}$$

a sensor is categorically *wideband* if its relative bandwidth is $0.1 \leq Q < 0.5$, and *ultra-wideband* if its relative bandwidth is $0.5 \leq q \leq 2$ [7,8].

ARL's UWB SAR operates across a 950-MHz-wide band, from 50 MHz to over 1 GHz (as determined by the 3-dB points for the antenna and digital oscilloscope, respectively), and thus has a relative bandwidth in excess of 1.8. A BASS103 (bulk avalanche semiconductor switch) is used as the transmitter, and drives a TEM horn antenna that effectively differentiates the 1-ns transmit pulse to form the radiated signal. Peak power is 500 kW; with a pulse repetition frequency of 40 Hz, the average transmitted power is about 20 mW. Figure 2 shows the through-the-air (transmitter to receiver) doublet generated by the system, with the spectral distribution shown in figure 3.

**Figure 1. UWB data-collection schematic.**
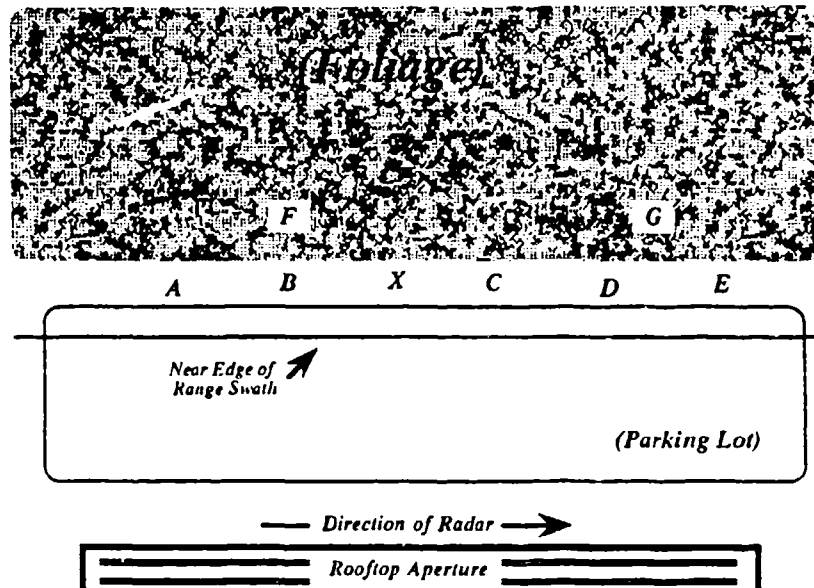


**Figure 2. UWB transmitted pulse.**

Figure 3. UWB pulse spectrum.
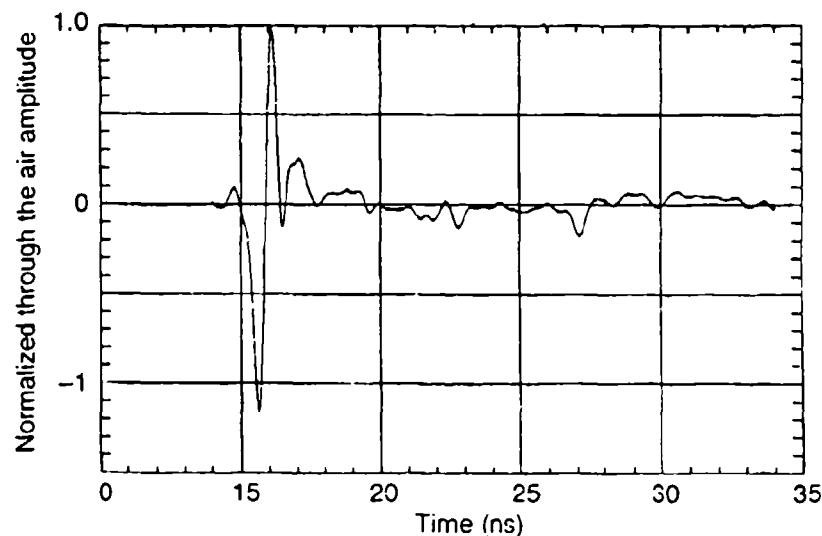


Figure 3. UWB pulse spectrum.
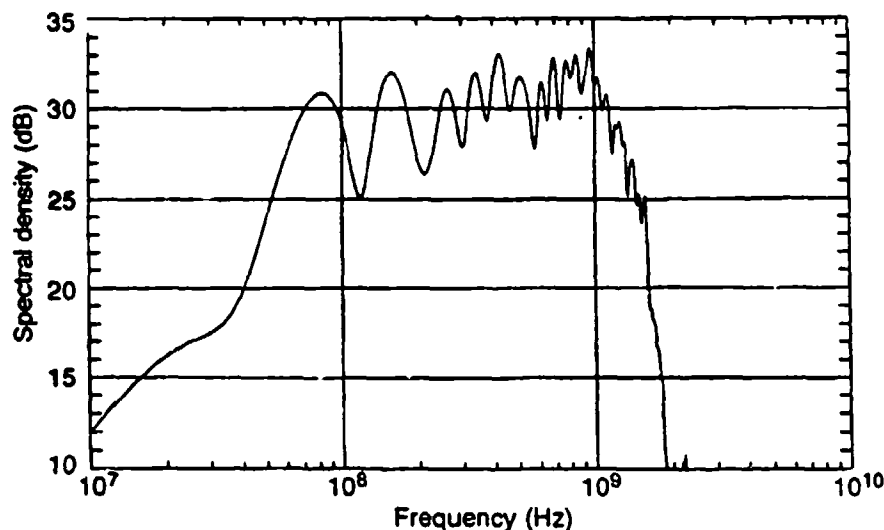
### 2.2.2 UWB SAR Image Formation

The ARL UWB SAR does not use the conventional two-dimensional (2-D) inverse fast Fourier transform (FFT) to create the radar image. Since the UWB SAR collects data in the near field and operates in the ultra-wide band, conventional Fourier processing must be restricted to very small patches within the image area, and becomes computationally intensive while not yielding a superior quality image. For these reasons, UWB SAR images are formed by a variant of the backprojection algorithm commonly used in medical imaging. (See app A for a description of the wide-band- and near-field-related pitfalls in Fourier image formation, as well as a brief description of the backprojection algorithm.)

## 2.3 Resonance Effects from Wideband Excitations

### 2.3.1 Wideband RCS

In the narrowband case, a target's echo is typically modeled as a scalar number ($\sigma$), the radar cross section (RCS) of the target. In general, however, RCS is a function of wavelength, phase, aspect angle, and polarization state. Wideband analysis thus motivates a revised definition of $\sigma$ as a complex quantity, with both magnitude and phase components [7,9]. In the time domain, the complex RCS can be represented as a ringing or resonant response of the target. If this resonant "signature" is sufficiently unique, the target can be modeled—and recognized—by spectral analysis of its resonant response [9–12].

## 2.3.2  Target Resonance Effects

The response of a resonant scatterer to an incident wideband pulse will generally be composed of two temporally distinct parts, referred to as the early-time response and the late-time response. The early-time response—or driven response—is the echo of the incident pulse, caused by local currents driven on the surface of the object; alone, it does not convey a great deal of information about the scatterer. The late-time response—also referred to as the resonant or impulse response—is a ringdown of the natural frequencies of the target excited by the incident pulse. These natural frequencies are a function of the electrical dimensions of the object.

The late-time resonance phenomenon is best illustrated through a canonical example. The spatio-temporal distribution of current along a thin-wire dipole of length $L$ is described by

$$i(x,t) = I_0\, e^{-at} \sin\!\left(\frac{2\pi x}{\lambda}\right) \sin\!\left(\frac{2\pi c t}{\lambda}\right), \qquad (4)$$

where $I_0$ is the value of the current at a current antinode [13,14]. Boundary conditions require $i(x,t) = 0$ at $x = 0$ and $x = L$, which lead to the condition $2\pi L/\lambda = k\pi$, $k = 1, 2, \ldots$. For $x = L/2$, substituting $\omega$ for $2\pi c/\lambda$ in (4) and using the relation $L/\lambda = k/2$, we obtain

$$i(L/2,t) = \frac{1}{n^2}\, e^{-at} \sin\!\left(\frac{\pi k}{2}\right) \sin(\omega t), \quad k = 1, 2, \ldots . \qquad (5)$$

Clearly, $i(L/2,t) = 0$ for $k$ even; these are the cases where the current distribution is antisymmetrical along the dipole (thus, no energy is radiated). Meaningful solutions to equation (5) exist for $k$ odd (henceforth referred to as *radiating harmonics*); these are the fundamental ($k = 1$) and higher ($k = 3, 5, \ldots$) harmonic resonances of the dipole. Note that $I_0$ in equation (4) has been replaced by $1/n^2$ in equation (5), indicating that the initial amplitude of the current flow is wavelength dependent [15,16]; this yields radiated-field strengths that scale with wavelength. The initial strength of the radiated field at each harmonic will be linearly proportional to the amplitude of the surface current, and will be governed largely by the $Q$-factor of the dipole at that frequency [17]. The $e^{-at}$ factor in equation (5) indicates that the current decays with time, unless the forcing function that initiated the current flow is reapplied. Since we are considering only late-time effects, we can assume that the forcing function has been removed, and the current will decay at a rate proportional to $a_k$—also known as the *damping factor*. The subscript $k$ on the damping factor indicates that the damping is frequency dependent; spe-

cifically, higher frequency components have greater damping than lower frequency components [3].

If the index $k$ in equation (5) is redefined as $n = (k + 1)/2$, the radiating harmonics of a dipole of length $L$ are defined by equation (6). Although $\omega$ is continuous in equation (5), it is effectively quantized at the radiating harmonics by the $\sin(k\pi/2)$ term; this is indicated by $\omega$ being indexed with $n$ in equation (6):

$$i(L/2, t) = \sum_{n} \frac{1}{n^2} \exp(-a_{\omega_n} t) \sin(\omega_n t) . \tag{6}$$

Thus, if a dipole in empty space is illuminated by a copolarized incident pulse, resonances at the odd harmonic components within the band of the illuminating pulse [1,11] will be excited, and will decay exponentially once the forcing function has been removed. For example, consider a resonator illuminated by a wideband pulse occupying a band from $f_{lo}$ to $f_{hi}$; if the resonator has a fundamental harmonic at $f_0$ and radiating harmonics at $f_n = n f_0$, $n = 1, 2, 3, ...,$ then the resonator's response will be described by

$$R(t) = \sum_{n} \Delta(f_n) A_n E_n(t) \sin(2\pi t) u(t), \quad \Delta(f_n) = \begin{cases} 1 & f_{lo} \leq f_n \leq f_{hi} \\ 0 & \text{otherwise} \end{cases}, \tag{7}$$

where $A_n$ is the maximum amplitude and $E_n(t)$ is the time decay of the $n^{th}$ harmonic component of the response, and $u(t)$ is the unit-step function.

Since the dipole is symmetric with respect to a plane oriented normal to the dipole's major axis, it will behave identically at all aspect angles within the plane, yielding a signature that is aspect-angle invariant. Anisotropic objects will typically provide signatures that are modulated to greater or lesser extent by the aspect angle between the source and the scatterer. This topic is discussed in greater detail in section 2.3.3.

If we now consider a complex target composed of multiple resonant "surfaces," we can model the target as a linear network of individual resonators. Linearity allows us to apply superposition: the response of the overall system is the linear sum of the responses of the individual resonant elements, and equation (7) can be generalized as

$$R(t) = \sum_{m=1}^{M} \sum_{n} \Delta(f_{m,n}) A_{m,n} E_{m,n}(t) \sin(2\pi f_{m,n} t) u(t) \tag{8}$$

14

for $M$ resonant structures in the illuminated target. If we assume that the resonant frequencies of the target are unique to that class of object, then the target can be clearly identified by its resonant signature [2,9-12]. While the uniqueness assumption is not likely to be valid for narrowband illuminations, it becomes more realistic as the bandwidth of the illuminating pulse increases [11]. Of course, the transmitted signal need not be an impulse—but it must, at a minimum, span the range of significant resonant components [1].

## 2.3.3 Phenomenology of Wideband Target Signatures

### 2.3.3.1 Incidence-Angle Dependence

Since most realistic targets are not isotropic, their signatures can be expected to vary with aspect angle. While the signature's *intensity* is often substantially modified by changes in aspect angle—even for relatively "simple" targets (fig. 4)—the impulse response remains largely invariant, except for attenuation effects such as shadowing [11,12]; similar statements hold for depression angle. Thus, while intensity-based ATR algorithms require many target "templates," representing critical increments in aspect and depression angles, a single resonance-based template—with an ATR algorithm designed to accept attenuated (or missing) components—should perform adequately at all angles of view. (The term "template" is used somewhat loosely here in spectral-analysis references.) This reduces the storage requirements of the ATR processor, and, with only a single template to consider for each target, processing requirements are reduced as well. These improvements can be critical in applications that need real-time, on-board processing capabilities.

This does not suggest that aspect-angle modulation of the resonant signature is insignificant: as shown elsewhere [11], spectral attenuation across various look angles can exceed 20 dB (fig. 5). These effects, however, are expected to be less pronounced in the impulse-response case than they are in the intensity-plot case, which is subject to cardinal aspect angles (where the signature needs to be

Figure 4. 20° double cone: (a) geometry and (b) measured backscatter cross section [18].

(a)

(b)



$\sigma/\lambda_0^2$ (dB)

Aspect angle (°)

15
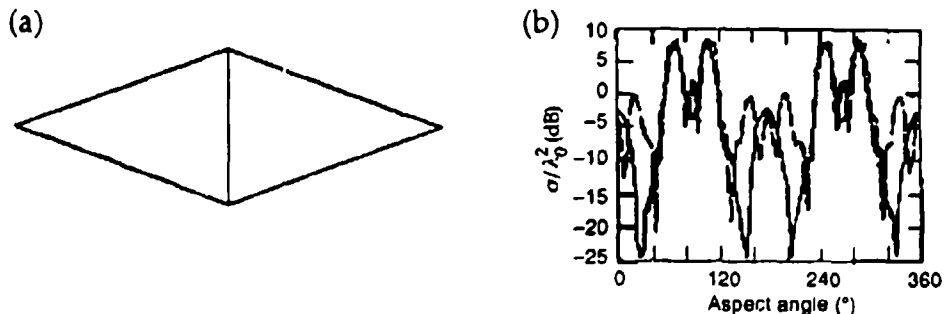
**Figure 5. Measured RCS of 1/72-scale model of an aircraft for three different angles of incidence (0° incidence is nose-on) [11].**

Measured RCS (dBsm)

0.0
-10.0
-20.0
-30.0
-40.0
-50.0

90°
45°
0°

Angular frequency $\left(\frac{\omega L}{cx}\right)$

0.0  0.2  0.4  0.6  0.8  1.0  1.2  1.4  1.6
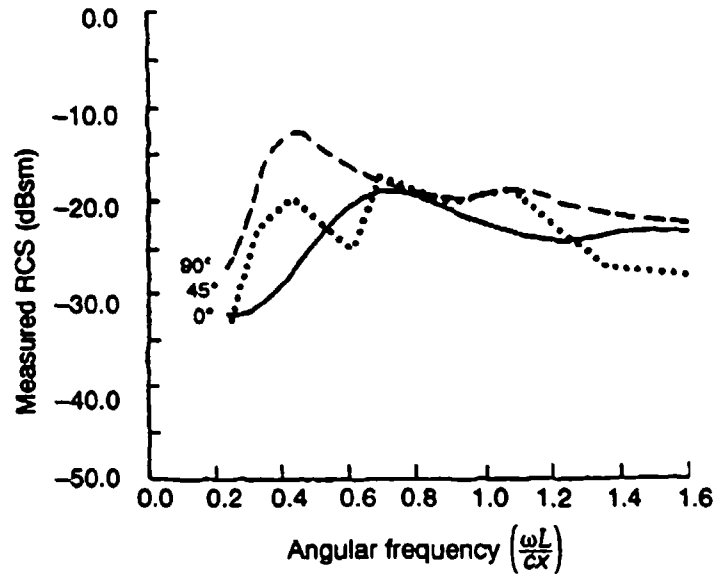
sampled more frequently with angle), "hot spots" (which may require high dynamic-range templates), and specular flashes (a combination of both problems). Thus, incidence-angle modulation of the target signature should be easier to accommodate in the spectral-analysis domain than in the intensity-based domain.

### 2.3.3.2 Polarization Effects

Another consideration in target modeling is polarization. A target's RCS can change significantly with polarization state [9], as shown in figure 6. In the impulse-response domain, polarization effects can modify the resonance states excited within the object by the incident pulse. These effects tend to attenuate—or even eliminate—specific components of the impulse-response signature [11]; thus, a robust ATR algorithm will have to account for these effects when processing target signatures.

The combination of aspect-angle dependence and polarization effects on a target's impulse response can be significant; for example, there may exist no combination of aspect angle and polarization state that will excite all critical resonances within the object, and some combinations may yield little or no response at all. However, in situations in which the target's resonant response is severely attenuated or absent, it is reasonable to assume that the intensity plot will have a correspondingly weak or missing signature, since the RCS of the object will be greatest at the resonance points [11]. In fact, resonance-point enhancement of RCS may yield adequate spectral signatures (albeit weak) in instances where there is insufficient broad-spectrum return for an intensity-based ATR algorithm to reliably detect the presence of the target.
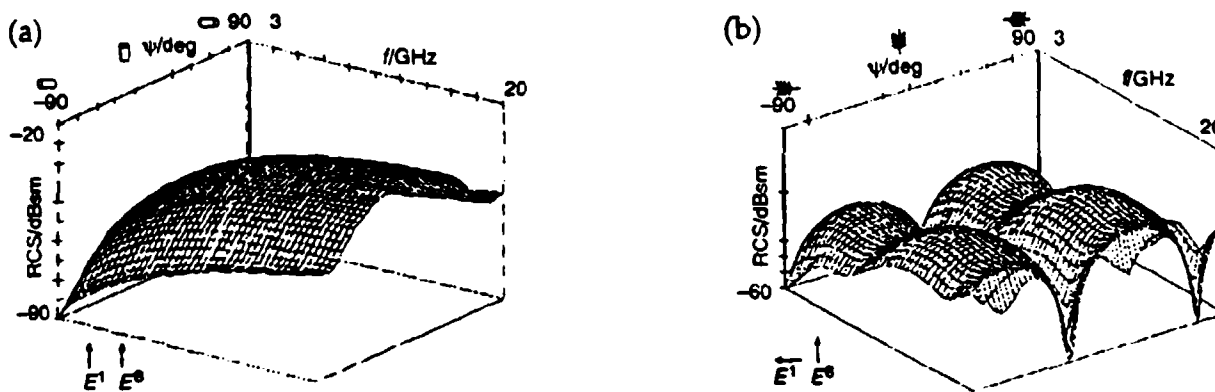
Figure 6. Dispersive polarimetric signatures: (a) copolarized lossy dielectric cylinder, and (b) cross-polarized spruce twig (*picea abies*) [9].

Independent of aspect angle and polarization state, modifications to the spectral signature are possible through operational alterations and environmental effects (damage to resonant elements, particularly those elements contributing dominant resonances) [11]. While it is not the intent of this report to address these issues, any robust target-recognition scheme must be capable of accounting for these signature modifications, whether the scheme is a template-based intensity correlator or a resonance-based spectral analyzer.

### 2.3.4 Signature Uniqueness

As discussed previously (sect. 2.3.2), the resonant-signature uniqueness assumption is not likely to be valid for narrowband illuminations, but becomes more realistic as the bandwidth of the illuminating pulse increases. Another factor in signature uniqueness is the number of clearly distinguishable resonant structures within the target (that is, structures that contribute dominant resonances) [11]. Obviously, it is essential that the radar band span the range of key resonances to be used in the ATR process. The significant resonant frequencies of most targets lie in the 2-MHz to 1-GHz range [12]; since ARL's UWB SAR spans most of this band, most significant components should be contained in the target resonant signatures from this radar.

Problems will arise when spectral signatures from differing target classes have significant cross correlations. In these instances, some secondary form of processing (contextual analysis, neural-net processing, human reasoning) may be required to declare an object as belonging to a specific class of targets. Preliminary studies, however, have indicated that there is sufficient spectral disparity—even among similar objects within the same target class—to differentiate

17

among complex objects [11]. This is an area that will benefit from continued investigation to validate the potential for reliable resonance-based ATR, and to compile databases of target resonant signatures.

## 2.4    Image-Analysis Methods

### 2.4.1    *Intensity-Based Algorithms*

In intensity-based pattern-recognition algorithms, a target model— or "template"—is constructed based on observations of the target's signature and signature characteristics (variance, sensitivity to external factors, etc.) and is generally used as the basis for some form of correlation operation on the data set. That is, the template is compared to the data set at some subset of points within the data, and a threshold is generally established (usually based on observation of the template's performance) to define the point at which a template/ data match is "good" enough that we can declare a target recognized. Since the target's intensity signature is typically substantially modulated by changes in aspect and depression angles [9,18], good correlation performance most often dictates construction of a separate template for each combination of critical-angle increments in aspect and depression.

This approach can yield substantial processing requirements. Consider the following example: a typical ATR algorithm may require templates at an average of every 5° in view angle for both azimuth and elevation. A SAR with a 30° field of view in elevation will thus require 6 *sets* of templates—each set containing 72 azimuth-angle-dependent templates at a specific depression angle—for a total of 432 templates. If the resolution is 1 m in both range and azimuth, and typical targets for that system are 3 by 8 m, then a *minimum* of 24 pixels is required for each template, totaling more than 10,000 pixels of stored data. Although the storage requirements are not significant, the pixel processing required to declare a target can be substantial. Algorithms vary widely in efficiency, but if we consider a system optimized to 100 operations per processed pixel (including overhead), and assume that an average of 216 templates (50 percent) must be processed for every target cue supplied to the recognition engine, then 500,000 operations are required for every potential target. Furthermore, if the detector supplies an average of 2000 target cues per image, 1 giga-op will be required to process only the target recognitions (computational order for the target cuer is not considered here). If the system resolution is increased to 0.333 m in range and azimuth, these figures increase by *at least* a factor of 9. In addi-

tion, many of the more elaborate target-recognition algorithms require templates that are larger in extent than the targets—generally for background contrast matching—resulting in even greater computational order. While advances in computer technology are bringing real-time processing capabilities within reach of the computational requirements, there still must be a significant investment made in processing power, weight, volume, and cost. A more efficient means of achieving the target-recognition goal would be beneficial in these applications.

## 2.4.2 *Spectral-Analysis Algorithms*

Ideally, we would like to model a target's signature with a single, aspect-angle-independent template. While this may not be an attainable goal for pattern-matching schemes, spectral-an⸱⸱ sis methods provide the potential to reach this objective.

In the spectral-analysis approach, the target is modeled by its key natural resonances, requiring a significantly smaller set of numbers to characterize the target [1,3,10–12,15]. The methods typically employed in extracting the complex natural resonances (poles) of the target are some variations on the algorithm proposed by Prony (circa 1795) [11,19–22]. (See ref 17 and 20 for translations of Prony's original work.) The following is a brief description of the Prony method of singularity extraction, and the limitations inherent in the method.

### 2.4.2.1 *The Prony Method*

The continuous-time transient scattered field from an object in empty space is defined by

$$E(t) = \sum_{i=1}^{M} A_i e^{s_i t} , \qquad (9)$$

where $M$ is the system order (the number of modes in the object's response); this field is then discretized over $N$ samples [1,21]:

$$E[n] = \sum_{i=1}^{M} A_i e^{s_i n T}, \quad 0 \le n < N . \qquad (10)$$

Here, the $\{s_i\}$ are the complex poles—i.e., the $\sigma_i = \sigma_i \pm j\omega_i$, where the $\sigma_i$ are the damping ratios and $\omega_i$ are the resonant frequencies—the $A_i$ are complex residues of each harmonic component, $T$ is the constant sample period, and $N$ is the total number of samples. Equation (10) represents $N$ simultaneous nonlinear equations in $2M$ un-

knowns ($M$ complex poles $\{s_i\}$ and amplitudes $\{A_i\}$); clearly, a unique, consistent solution exists only for $N \geq 2M$. If this requirement is met, the set of simultaneous equations in (10) can be solved by Prony's method. This method is based on the fact that equation (10) can be modeled as a polynomial,

$$\sum_{m=0}^{n} \alpha_m Z^{M-m} = 0, \quad \alpha_0 = 1 , \tag{11}$$

whose coefficients can be obtained from a simple difference equation:

$$e_k = -\sum_{m=1}^{n} \alpha_m e_{k-m} , \quad \Pi \leq k < N , \tag{12}$$

where $\Pi$ is the *estimated* order of the system (the system order is generally not known *a priori*). If exactly $2\Pi$ samples were taken, then equation (12) is solved exactly for the $\alpha_m$; if the data are oversampled ($N > 2\Pi$), then a least-squares type of fit will be required for the $\alpha_m$ to be obtained. Once the $\alpha_m$ have been determined, the roots of equation (11)—which describe the natural resonances through $Z_m = e^{s_m T}$—define the poles of the model:

$$s_m = T^{-1} \ln Z_m . \tag{13}$$

Now, inserting the poles $\{s_m\}$ into the system of equations in (10) linearizes the system, and solving for the residues $A_i$ is straightforward.

This method is very sensitive to noise, and loses even more noise immunity when multipath effects are factored in [11,21]. Even without multipath considerations, a brief survey of the literature reveals that a substantial effort has been undertaken to find solutions to the noise-immunity problems in Prony [20,22-26]. As discussed above, a least-squares fit will be required if the system is oversampled; if there is noise present in the system, however, it will significantly perturb the least-squares solution, since noise does not fit the causal model of the system [3]. Furthermore, if the estimated order of the system, $\Pi$, is greater than the actual order, $M$, the solution will contain poles due entirely to noise. Prony provides no means of distinguishing these poles from the real system poles. Similarly, if the estimated order is less than the actual order, the "excess" poles will be lost, and the remaining poles will be perturbed by their positions [3]. These shortcomings severely limit the efficacy of Prony's method in applications with signal-to-noise ratios below about 15 to 20 dB [2].

Poor noise immunity notwithstanding, the Prony method is also computationally intensive, as is easily inferred from the formulation of the method (eq (9) through (13)); inclusion of multipath effects serves to substantially increase the algorithmic complexity. These shortcomings motivate spectral-analysis methods with reduced computational order and greater noise immunity than Prony. We believe that linear transforms—such as Fourier and wavelets—provide the desired solutions to these shortcomings. It will be shown that the multiresolution bases, in particular, model the decay characteristics of complex resonant excitations more effectively than does the Fourier transform, and thus yield superior performance in detection of target ringdowns.

### 2.4.2.2  The Fourier Transform

The Fourier transform is very familiar in signal processing; thus, its derivation here is unnecessary (the reader is referred elsewhere [27–30]). However, the discrete Fourier transform (DFT) and its computationally optimized counterpart, the fast Fourier transform, exhibit some specific characteristics that warrant brief discussion.

Consider a real, continuous-time periodic signal $x(t)$, with maximum frequency $f_{max}$ and period $T$ (i.e., $x(t) = x(t + kT)$ for any integer value of $k$). We can discretize this signal by sampling at a constant rate $f_s \geq 2f_{max}$, yielding the discrete sequence $x[n]$. Taking $N$ to be the fundamental period of the discretized signal $x[n]$, we can define the DFT of $x[n]$ by

$$X[k] = \sum_{n=0}^{N-1} x[n] \, W_N^{nk}, \quad W_N = e^{-j(2\pi/N)} \; ; \tag{14}$$

the function $W_N$ is an artifice of convenience. For an illustration of the distribution of the spectral coefficients $X[k]$, consider the Z-transform of a single period of $x[n]$:

$$X[z] = \sum_{n=0}^{N-1} x[n] \, z^{-n} \; . \tag{15}$$

Comparing (14) and (15), we can see that the spectral coefficients $X[k]$ and $X(z)$ are related by

$$X[k] = X(z) \big|_{z = W_N^{-k}} , \tag{16}$$

where $W_N^{-k} = e^{j(2\pi/N)k}$ . The $(2\pi/N)$ term in the argument of the exponential divides the unit circle by $N$, and the index $k$ then steps the analysis frequencies around the unit circle in equi-angular incre-

ments. Thus, the DFT corresponds to $N$ equally spaced samples of the z-transform around the unit circle (fig. 7) [29]. This yields equally spaced analysis frequencies, as well as analysis subbands of constant bandwidth. By the definition of relative bandwidth in equation (3), Fourier subbands can be said to exhibit variable relative bandwidth; this is also termed "variable-$Q$" analysis. We can achieve finer resolution in frequency (smaller subband bandwidths) by increasing $N$, i.e., increasing the number of samples in the analysis window; this decreases the time localization of the transformed spectral information. Thus, resolution in time and frequency are inversely proportional, and are determined by the length of the analysis window selected.

It is worth noting that this formulation is independent of the sampling frequency, $f_s$, which corresponds to the $2\pi$-radians point on the circle. The point at $\pi$ radians then represents the maximum permissible spectral component of the original continuous-time signal $x(t)$. This implies that the DFT coefficients that lie entirely in the third and fourth unit-circle quadrants (represented by $k = 5, 6, 7$ in fig. 7) do not contain any unique information; in fact, they are conjugate-symmetric points to those that lie above the abscissa, which is clear from the definition of $W_N$ [30]. Therefore, these points represent redundant information for $x[n]$ a real function.

Generalizing $x[n]$ to be a complex sequence, we can rewrite the DFT as

$$X[k] = \sum_{n=0}^{N-1} \left\{ \left( \text{Re}(x[n])\text{Re}(W_N^{kn}) - \text{Im}(x[n])\text{Im}(W_N^{kn}) \right) + j\left( \text{Re}(x[n])\text{Im}(W_N^{kn}) + \text{Im}(x[n])\text{Re}(W_N^{kn}) \right) \right\}, \quad k = 0,1,... N - 1 ; \quad (17)$$

Figure 7. Z-plane samples of z-transform (for $N$ = 8) which correspond to coefficients of discrete Fourier transform [30].
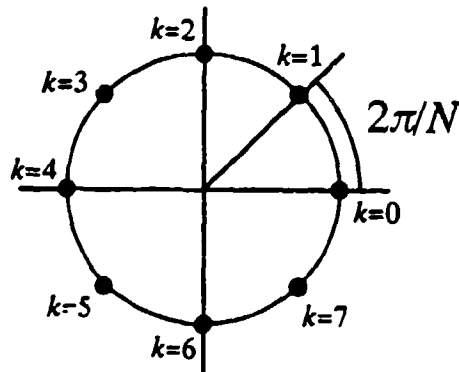
from this, the computational order of the DFT is seen to be proportional to $N^2$, whether $x[n]$ is real or complex (there is a factor-of-two reduction for $x[n]$ purely real, because the $\text{Im}(x[n])$ terms drop out, but the computational order remains $N^2$).

Exploiting the symmetry and periodicity properties of $W_N$, Cooley and Tukey [31] devised an optimization of the DFT, reducing the computational order to $N \log_2 N$. This optimization, now termed the fast Fourier transform (FFT), is widely discussed and derived in introductory signal-processing texts [29,30]. The interpretations of the DFT spectral coefficients, analysis windows, subband bandwidths, and frequency resolution apply directly to the FFT; the only difference is the computational order.

Another formalism in Fourier signal-processing theory is the short-time Fourier transform (STFT), which is an FFT preceded by a weighting function (window). If the window is rectangular, the STFT reduces to a simple FFT. The maximal time-frequency concentration characteristics of Gaussian functions led Gabor to propose them as weighting functions in 1946 [32]; STFT functions wit'. Gaussian-weighted windows are referred to as "Gabor wavelets" [33].

### 2.4.2.3 Nonstationary Signal Analysis

Fourier processing is well suited to the analysis of stationary signals with a limited number of components (i.e., sinewaves) spaced over a relatively narrow band in frequency. If the relative bandwidth of the signal becomes large, however, certain inefficiencies become apparent. Specifically, variable-$Q$ analysis methods have either poor time localization (with unnecessary frequency resolution) at the high end of the band if relatively long analysis windows are used, or poor frequency resolution (with unnecessary time localization) at the lower frequencies if relatively short analysis windows are used. Compromises are possible, but the above statements still hold in general; furthermore, the situation deteriorates as the relative bandwidth increases.

Consider, for example, an acoustic signal generated by a piano key being struck: the sustainment of the signal will be composed of fast decaying high-frequency harmonics and slowly decaying low-frequency harmonics (the quickly decaying response is often referred to as the "attack" of the note). A three-tone example of this phenomenon is given by

$$x(t) = e^{-K\omega_1} \sin(\omega_1 t + \varphi_1) + e^{-K\omega_2} \sin(\omega_2 t + \varphi_2) + e^{-K\omega_3} \sin(\omega_3 t + \varphi_3) \; ; \quad (18)$$

23

the $K\omega_n$ term in the exponential indicates the frequency-dependent characteristic of the decay. There will also be a short driven response before the harmonic ringdown. The unforced decay is illustrated graphically in figure 8.

Both the driven response and the ringdown generally are wideband phenomena: acoustic signals can easily span several octaves, yielding relative bandwidths very near 2.0. Modeling the attack of the note through Fourier analysis is inefficient because of the nature of fixed-length analysis windows; one must either select short time windows to provide adequate temporal resolution of the transient characteristics of the signal—thereby sacrificing frequency resolution of the slowly decaying lower harmonics (which better characterize the resonant response than the higher harmonics [16])—or employ longer time windows, which fail to adequately capture the spectral characteristics of the discontinuity, and will yield poor temporal resolution of the event (fig. 9). Thus, Fourier analysis is suboptimal, at best, for analysis of wideband transient signals.

Signals such as these—fast decaying high-frequency components with slowly decaying low-frequency components—are often encountered in practice [32], and, in particular, characterize the wideband resonant-target responses discussed in section 2.3. A desirable method of analyzing these signals would capture the transient properties of the signal while effectively modeling longer term, slowly decaying characteristics. This requires a "multiresolution" approach to the problem: higher, quickly decaying components are analyzed with shorter, broader bandwidth windows (which are poorly resolved in frequency but well resolved in time); lower, quasi-stationary components are analyzed with longer, narrower bandwidth windows (poorly resolved in time, but well resolved in frequency). Decompositions such as these are often referred to as "multiresolution pyramids." The wavelet transform, which unifies much of the theory surrounding multiresolution methods, provides the potential to model wideband resonance characteristics with greater efficiency than the Fourier transform.

**Figure 8. Acoustic "attack" of a note.**



24
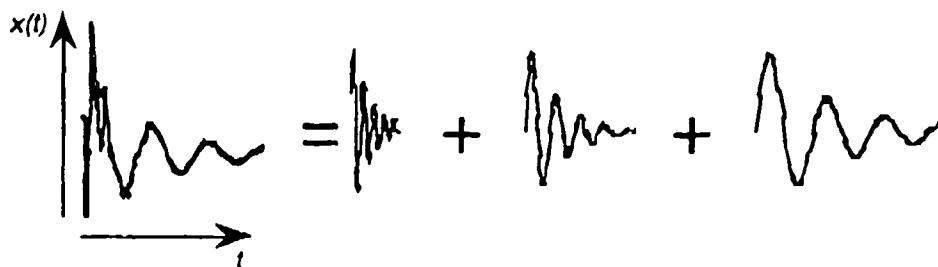
**Figure 9. Modeling attack of a note with Fourier (fixed) analysis windows: (a) shorter analysis windows provide good temporal resolution, and (b) longer analysis windows provide improved frequency resolution.**



(a)

(b)
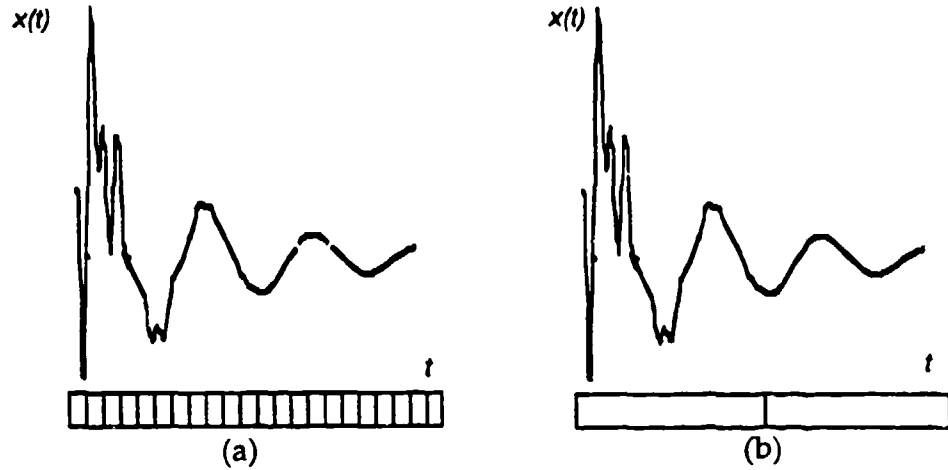
### 2.4.2.4 *The Wavelet Transform*

Although various concepts related to wavelet theory were expressed nearly a hundred years ago [34,35], the contemporary, unified formalism is a rather recent development in the signal-processing field. A substantial volume of wavelet-related literature has been produced in recent years—some of the better treatments can be found in the references [36–40]; also see Chui [41] for an excellent survey of recent papers on wavelet theory and applications. Hence, only the relevant concepts are developed in this discussion.

Described succinctly, wavelets are dyadic (power-of-2) dilations and translations of compactly supported functions; they may also be mutually orthogonal, although this is not a requirement. Consider a set of functions $h_{a,b}(t)$, defined as

$$h_{a,b}(t) = \frac{1}{\sqrt{|a|}} h\left(\frac{t-b}{a}\right), \quad a, b \in \mathbf{R}, \quad a \neq 0 , \tag{19}$$

where $h$ is supported over some closed interval $I$, with $h = 0$ elsewhere. Let $V$ be defined as the space of signals with finite energy, $V \subset L^2(\mathbf{R})$ (henceforth referred to as the signal space), where $\mathbf{R}$ is the set of real numbers, and $L^2(\mathbf{R})$ denotes the space of real numbers with dimensionality 2, considered as one geometric whole. If the $h_{a,b}$ span the signal space such that they form an orthonormal basis in $V$,

$$\int h_{a,b}(t) h^{*}_{a',b'}(t) \, dt = \begin{cases} 1, & a = a' \text{ and } b = b' \\ 0, & \text{otherwise} \end{cases} , \tag{20}$$

25

then an arbitrary signal $x(t)$ can be represented as a linear projection onto this basis. The projection, or decomposition, of $x(t)$ onto the basis is represented simply as a weighted sum of basis functions:

$$x(t) = \sum_{a,b} c_{a,b} h_{a,b}(t) \ . \tag{21}$$

A necessary condition for the existence of a unique solution to (21) is that the $h_{a,b}$ are square-integrable functions; this condition is met if $h$ is square integrable [37,39].

Analyzing (19), we can see that the index $a$ governs the time basis for the function $h$, which can be interpreted inversely as frequency; this behavior is illustrated in figure 10. For $|a| > 1$, the time basis is contracted, and function $h_{a,b}$ is extended over a greater interval (fig. 10b); this, of course, serves to lower the frequency components inherent in $h$. Similarly, for $|a| < 1$, the time basis is expanded ("dilated"), and $h_{a,b}$ is contracted proportionally; this shifts the spectral components of $h$ to a higher frequency range. For $|a| < 1$, $h_{a,b}$ "lives" on a shorter interval (fig. 10c) than it does in the $|a| > 1$ and $|a| = 1$, and thus does not span the entire interval; this is equivalent to not spanning the signal space $V$. We can ensure the span of $V$ by translating the function within the interval so as to ensure that the interval is spanned at all points; this is shown in figure 11 (note that

**Figure 10.**
**Contractions and dilations of $h$: (a) $|a|$ = 1 (unity time scaling), (b) $|a| > 1$ (contraction), (c) $|a|$ < 1 (dilation).**



(a)

(b)                    (c)
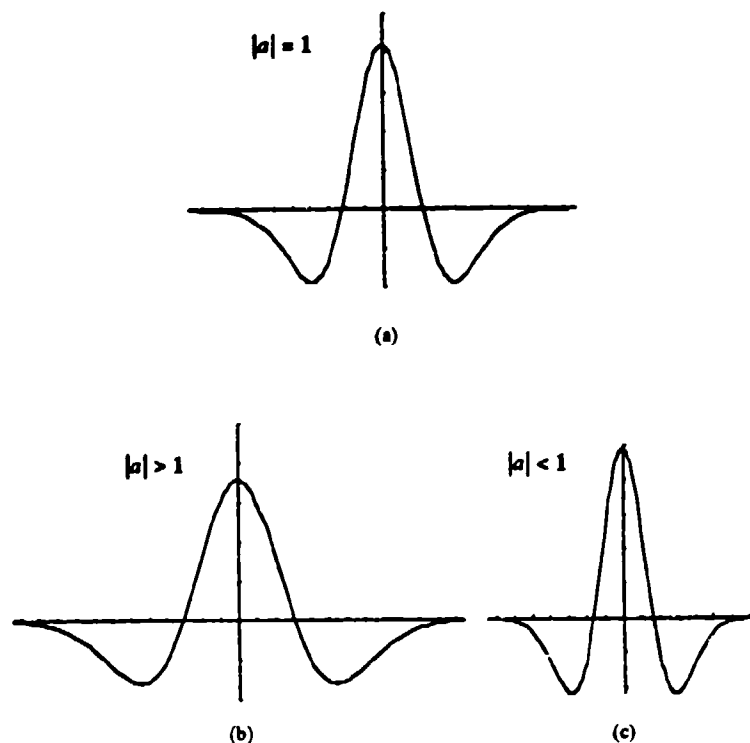
this does not ensure the orthogonality of the spanning set). Thus, higher dilation levels—representing higher frequency oscillations—require more translations to ensure the span of $V$.

Since the basis functions $h_{a,b}$ are not constrained to be sinusoidal, they are generally wider band than their sinusoidal Fourier counterparts (in comparison, the Fourier basis functions are impulses in frequency space). For this reason, the notion of *scale* is introduced in wavelet analysis: higher dilation levels, which loosely correspond to higher frequency bands, are designated as smaller scales; less dilated functions correspond to larger scales.

Up to this point, we have not constrained the values of the parameters $a$ and $b$ (except that $a$ must be nonzero). In signal-processing applications, however, there is a natural discretization of these parameters: consider two scales $a_1$ and $a_2$, such that $a_1 < a_2$; these scales correspond to two frequency bands, $\Delta f_1 > \Delta f_2$. If, in fact, $\Delta f_1 = 2\Delta f_2$, then the data at scale $a_2$ can be decimated by a factor of 2 (assuming one-dimensional, discrete data). Applying this recursively, we see that dyadic dilations yield convenient results for discrete signal-processing applications; thus, we discretize the parameter $a$ as $a = 2^m$, where $m \in Z$ ($Z$ is the set of all integers). This also discretizes the parameter $b$: if the "primary time window" is defined as the interval spanned by the largest scale (least dilated) basis function among the $h_{a,b}$, the number of translations required to span the primary time window at any given scale is just the dyad level of the scale. That is, at scale $m$, $2^m$ translations are required to ensure the span of the signal space. This yields a sparsely sampled discrete sublattice with dyadic spacing in $V$, which is a very appealing result in most signal-processing applications [36,39].

The functions $h_{a,b}$ have characteristics similar to those of spatially confined waves, such as standing waves. Thus, the French geophysicist Morlet, who first proposed applications of these functions in the

Figure 11.
Translations of $h$:
(a) $|a| = 1$, $b = 0$ (no dilation, no translation), (b) $|a| = 0.5$, $b = 0$ (dilation with no translation), (c) $|a| = 0.5$, $b = 1$ (dilation with translation).



27
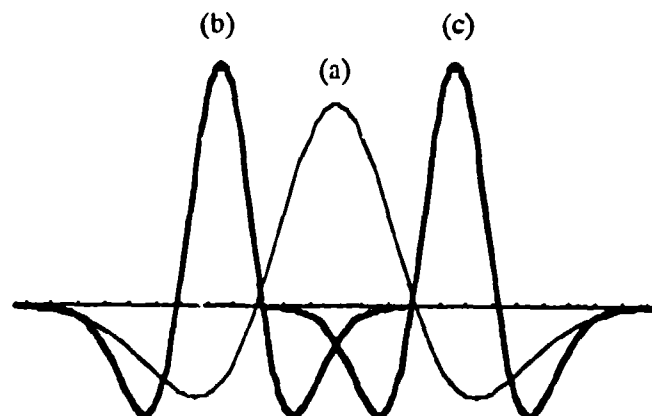
analysis of seismic data [42], referred to them as "wavelets of constant shape" (to contrast them with the Fourier basis functions, whose shapes change across subbands); this term was subsequently shortened to "wavelets." Finally, the wavelet at scale $m = 0$ is widely referred to as the *primary, basic, prototype*, or *mother* wavelet (since it gives rise—through successive dilations and translations—to the entire progeny of wavelets that constitute the wavelet basis). For orthogonal bases, the primary wavelet is generated as a modulation of a scaling function, which is a low-pass filter satisfying the "dilation equation" for $N$ coefficients $c_k$:

$$\varphi(t) = \sum_{k=0}^{N} c_k \, \varphi(2t - k) \; ; \tag{22}$$

the primary wavelet is then generated from [36,39,40]

$$W(t) = \sum_{k=0}^{N} (-1)^k c_{1-k} \, \varphi(2t - k) \; . \tag{23}$$

(Here, I use $W$ for dyadically scaled wavelet bases and $k$ for the translation parameter, notation commonly used in the engineering literature.)

As an example, consider the Haar basis. The Haar scaling function, which satisfies the dilation equation (22) with $c_0 = c_1 = 1$ ($c_k = 0$ elsewhere), is simply the "box" function (fig. 12a), supported here on the interval [0,1]. The Haar basic wavelet is then defined by equation (23) (fig. 12b). The infinite family of basis functions, defined by

$$W_{m,k}(t) = W(2^m t - k), \quad m \geq 0, \; 0 \leq k < 2^m, \quad m,k \in Z \;, \tag{24}$$

is shown in figure 13 for the first two dilations of the basic wavelet and their associated translations; the scale-dependence of the analysis-window length is distinctly illustrated in this figure. Clearly, any piecewise-continuous function (i.e., any sample-and-hold signal) can be represented by continually smaller analysis scales until the temporal support of the smallest scale is equal to the sample period of the signal Thus, the Haar basis should provide satisfactory performance in the analysis of most digitized signals, although it typically is not optimal.

Note that the wavelet basis is purely real, in contrast to the Fourier basis, which is complex. It is partly for this reason that wavelet bases are so computationally efficient: the Haar-basis transform can be reduced—through a butterfly operation similar to the FFT—to a computational order linear in $N$ [40]. This is substantially more efficient

28

**Figure 12. Haar scaling function (a) and basic wavelet (b).**

(a) $\varphi(t)$

(b) $W(t)$
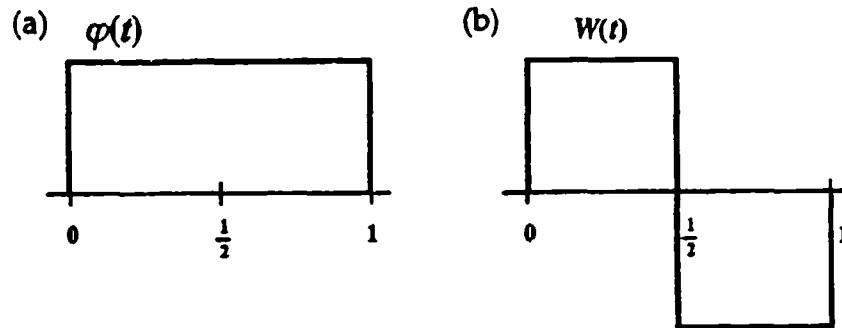
**Figure 13. First two Haar dilations and associated translations.**

$W_{1,0}(t)$

$W_{1,1}(t)$

$W_{2,0}(t)$

$W_{2,1}(t)$

$W_{2,2}(t)$

$W_{2,3}(t)$
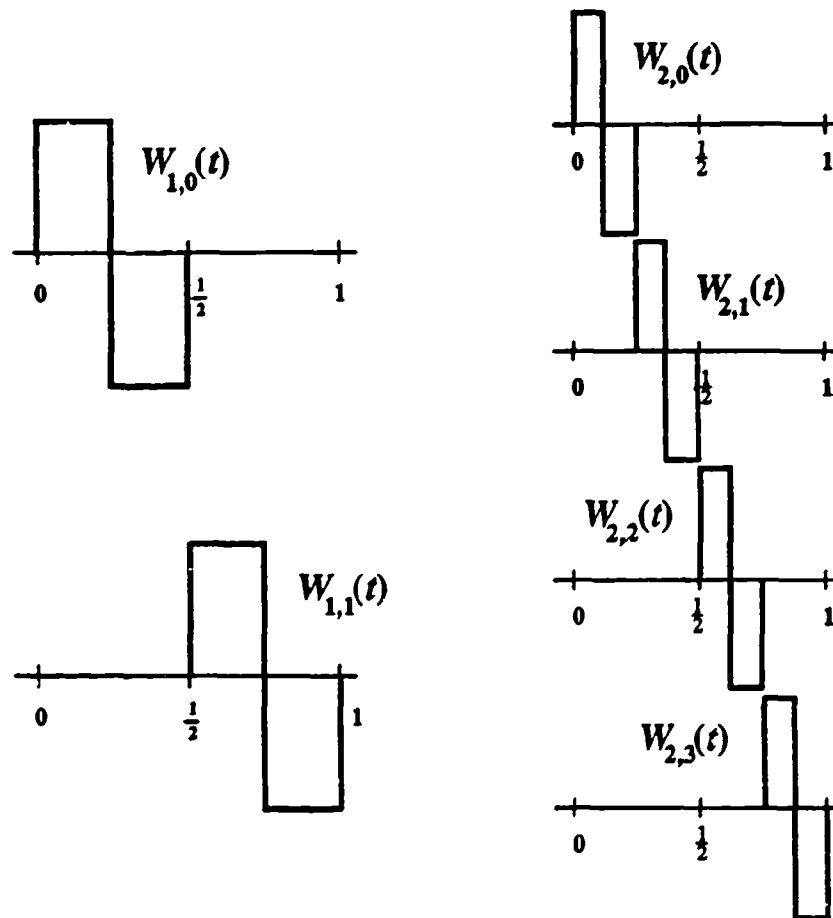
than the FFT, whose computational order is $N \log_2 N$. Although complex wavelet bases can be constructed (to recover phase information from the analyzed signal, for example), it is the real bases that are most often employed in wavelet-based signal-processing applications.

29

### 2.4.2.5 Wavelet Analysis

The time dependence of the spectral bands in both Fourier and wavelet analysis is best illustrated through introduction of the time-frequency plane. The essential concentrations of the basis functions in both time and frequency for both analysis methods are displayed in the time-frequency planes of figure 14. Note the dyadic time-scale tiling of the wavelet plane; it is this scaling that provides the wavelet transform's superior performance in the analysis of wideband, nonstationary phenomena. (The bottom row in fig. 14b represents the scaling (low-pass) function, for which the window size is identical to that of the primary wavelet, represented by the next higher row of tiles. For bases that do not have a corresponding scaling function, this row will be absent from the lattice structure.)

Let us now revisit the transient-signal modeling problem presented in section 2.4.2.3. Using the wavelet transform, we can efficiently model the discontinuity at the initiation of the transient. As depicted in figure 15, the smaller scales—well resolved in time—capture the fast high-frequency decays, while the larger scales—well resolved in frequency—effectively model the slowly decaying low-frequency components. Note that these signals are very similar to the wideband ringdowns described in section 2.3; thus, we expect the multiresolution transform methods to provide an effective basis for analysis of resonant target signatures in UWB SAR imagery.

**Figure 14. Time-frequency lattices: (a) Fourier basis, (b) wavelet basis.**
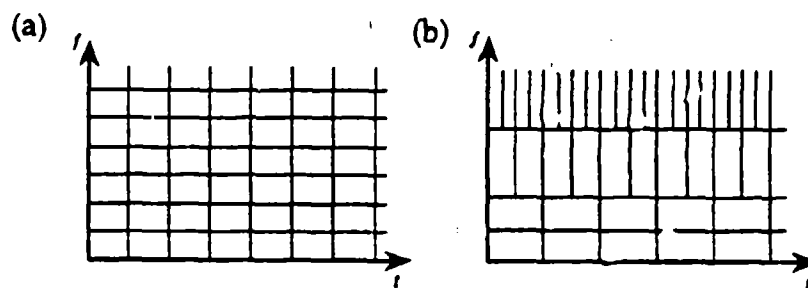


**Figure 15. Multiresolution modeling of transient phenomena.**
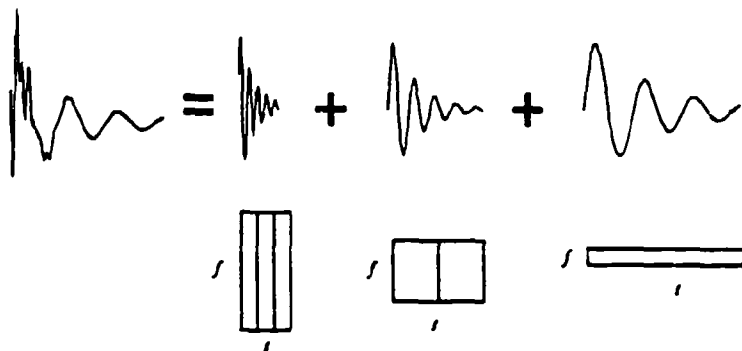
# 3. Target Recognition in UWB SAR Imagery

## 3.1 Prediction of Target Resonance Effects

It is always reassuring when the observed behavior of a system agrees closely with prediction; for this purpose, a predictive model must be constructed to describe and evaluate the behavior of the system under observation. For the purpose of this report, the canonical "target set" will be composed of two dipoles of different dimensions: a 166.4-cm dipole with a 7.62-cm-diam circular cross section, and a 114.3-cm dipole with either a 3.81-cm square cross section or a 5.08-cm-diam circular cross section (for reasons beyond the scope of this report, I consider only the 5.08-cm circular cross section when modeling the response of the 114.3-cm dipole). These targets were selected for th  straightforward predictability of their characteristic resonant responses to wideband excitations.

To predict the characteristic responses of the targets, I use the formulation developed in section 2.3. Equation (4) describes the distribution of current along a thin-wire dipole (diameter $d \ll L$); a suitable application of boundary conditions leads to the relation $\lambda = 2L/k$. This yields fundamental harmonics for thin-wire dipoles with $L = 114.3$ and 166.4 cm at 131.1 and 90.1 MHz, respectively. The thin-wire assumption, however, is not directly applicable in this case, since the cross sections of the dipoles used are significant [43]. The cor sequence of a nontrivial cross section is to increase the effective electrical length of the rod ("end effects") [43–45]. These corrections, described in detail elsewhere [43], are shown graphically in figure 16. For the dipoles under consideration here, $L/d$ is 22.5 for the 114.3-cm dipole, and 21.8 for the 166.4-cm dipole; these values correspond to correction factors ($K$) from figure 16 of approximately 0.945 in

Figure 16. Electrical-length corrections for dipoles of large cross section [45].



31
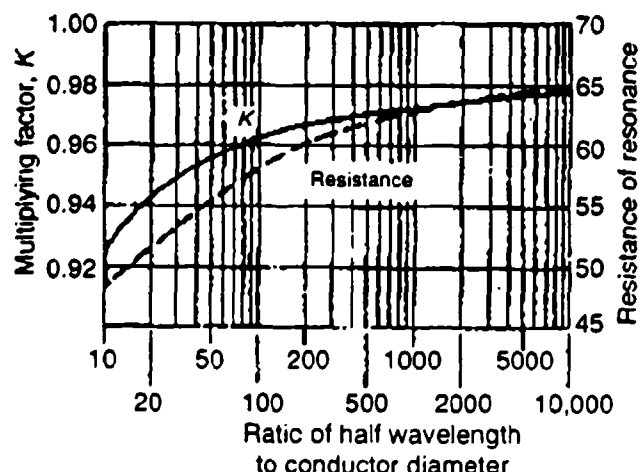
each case. The ratio of physical length to electrical length is $K$, which leads to the end-effect corrected equation relating the length of the dipole to the radiating harmonics:

$$\lambda = \frac{2L}{k}K^{-1} \ . \tag{25}$$

This yields fundamental harmonics at 124 MHz for the 114.3-cm dipole, and 85 MHz for the 166.4-cm dipole. The radiating harmonics within the band of the ARL UWB SAR for the 114.3-cm dipole are 124, 372, 620, and 868 MHz; similarly, the 166.4-cm dipole's radiating harmonics are 85, 255, 415, 585, 745, and 905 MHz.

As described in section 2.3.2, the resonant response should be preceded by a forced response, which is a reflection of the incident pulse caused by the pulse driving currents on the surface of the object. The amplitude of this response will be determined by those factors affecting the RCS of the object—phase, aspect angle, and polarization state. Once the incident pulse has transitioned past the surface of the object, the response will be characterized by the unforced decay of the natural resonances. Although the transmitted pulse is generally treated as having very fast decay characteristics, observation of the actual pulse radiated from the ARL UWB SAR antenna indicates that remnants of the static discharge continue to radiate from the antenna for a period lasting 15 to 20 times the duration of the initial pulse. These radiated remnants can drive currents on the surface of the object, continuing to excite specific harmonic modes, which may cause the excited modes to exhibit nonexponential decay behavior. This type of behavior has been observed in some of the data, and is discussed in section 3.2.2.

## 3.2 Empirical Assessments

### 3.2.1 Description of UWB SAR Imagery

Five different images were analyzed in the course of the research, each image representing a single polarization state. Transmit and receive polarizations are inclined 45° to the slant plane, as defined by their electrical planes. Since the rooftop aperture runs nearly due west-east, polarization states are designated as "west" (electrical plane inclined upward to the west) and "east" ($E$-plane upward east). Transmit polarization is stated first in the nomenclature; thus, an east-transmit, west-receive polarization channel is designated "EW."

The images are composed of 8 megapixels each—2K pixels in azimuth and 4K pixels in range—projected onto a Cartesian image

grid. The raw data are purely real; we obtain intensity plots by performing a Hilbert transform on the real data to generate a quadrature image, and calculating the scalar magnitude of the in-phase and quadrature images. This step effectively eliminates target resonant responses, so intensity plots are used only for display purposes; all target processing is performed on the bipolar SAR amplitude map.

Each image analyzed contains from one to four dipoles. Dipole-orientation designations follow a convention similar to that used for the polarization states: a dipole oriented upward to the east is referred to as an "east" dipole; those oriented upward to the west are "west" dipoles. "Vertical" and "horizontal" dipole orientations are referenced to the ground plane.

### 3.2.1.1 *Image 1: Run 1, WW Polarization, Four Targets*

The aperture run for the first image was made during the period from 11 to 20 January 1993. (About 80 hours are required to collect a single complete aperture of data.) Vegetation was devoid of foliage. The polarization of the analyzed image is west transmit, west receive. There are four 114.3-cm dipoles in the image, one each at the orientations of vertical (A), east (B), west (C), and horizontal (D), where the letters in parentheses denote locations of the targets in figure 1. This provides one dipole (west) in the polarization plane (i.e., copolarized), two dipoles inclined 45° to the plane (vertical and horizontal), and one dipole (east) orthogonal to the plane of polarization (cross-polarized). The dipoles were placed at slant ranges of 152.3 to 155.0 m, about 6 m in front of the tree line in range.

### 3.2.1.2 *Image 2: Run 2, EW Polarization, Four Targets*

Image 2 is identical to Image 1, except that cross-polarized data (east transmit, west receive) are employed. For dipole targets oriented 45° to the ground plane (east/west dipole), the signatures should be the result of single-bounce multipath (the bounce will occur on either the outbound or reflected pulse, depending on the orientation of the dipole), and should thus be substantially attenuated compared to similar direct-path signatures.

### 3.2.1.3 *Image 3: Run 4, WW Polarization, One Target*

The aperture run for the third image was made during the period from 20 to 28 April 1993. Vegetation was about 50-percent foliated. The image polarization is west transmit, west receive. There is one 114.3-cm dipole in the image (position E in fig. 1), oriented up east (cross-polarized), about 6 m forward of the tree line.

33

### 3.2.1.4 *Image 4: Run 6, WW Polarization, Two Targets*

The aperture run for this image was made during the period from 5 to 11 May 1993. Vegetation was about 70-percent foliated. The image polarization is west transmit, west receive. There is one 114.3-cm dipole in the image (position E in fig. 1), oriented up east (cross-polarized), about 6 m forward of the tree line.

### 3.2.1.5 *Image 5: Run 7, WW Polarization, Two Targets*

The aperture run for the fifth image was made during the period from 29 June to 12 July 1993. Vegetation was in full foliage. The image polarization is west transmit, west receive. In the image, there is one 166.4-cm dipole (position F) and one 114.3-cm dipole (position G), both oriented up east (cross-polarized). Both targets were placed in the foliage; the 166.4-cm dipole was placed about 9.1 m behind the tree line, and the 114.3-cm dipole was placed about 11.3 m behind the tree line. Both targets were entirely obscured by foliage.

## 3.2.2 *Observations of Target Ringdowns*

As discussed in section 3.1, radiating harmonics for the 114.3-cm dipole are expected to be seen at 124, 372, 620, and 868 MHz. Analysis of the west dipole in the WW-polarized data of Image 1 (fig. 17)—a combination that should yield the best response—reveals the presence of all four harmonic components, with very close agreement to prediction. The magnitude of each component scales roughly inversely with wavelength. The horizontal dipole exhibits similar characteristics. In these two cases, observation coincides well with prediction (sect. 2.3.2), although there are minor deviations; these are discussed in section 3.2.3.

**Figure 17. Range-line cut of west dipole in Image 1.**



34
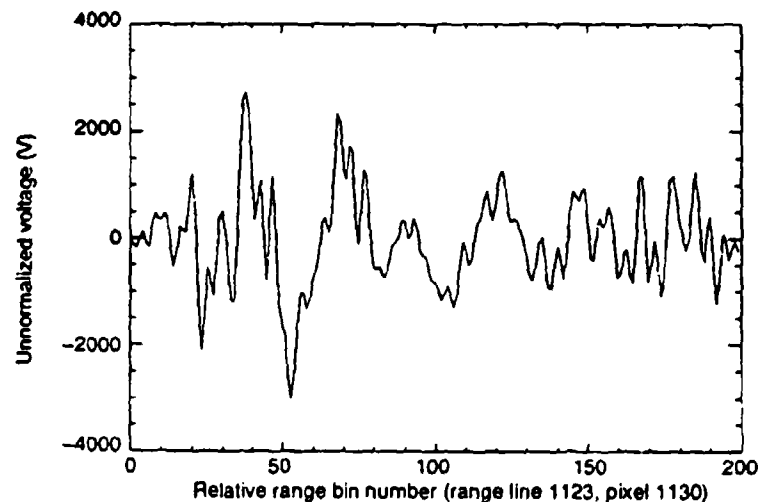
The primary (i.e., lowest frequency) components generally displayed approximately four "good" oscillations before the harmonic decayed into the noise.

The vertical and east dipoles do not correlate as well with the predicted response; deviations from the predicted response are presented in the next section.

### 3.2.3 Analyses of Deviations from Prediction

Observation of the data reveals some deviations from the predicted responses. The following is a summary of the observed deviations for the 114.3-cm dipole. Since the only data for the 166.4-cm dipole have the target cross-polarized to the image polarization plane, these were not used as a baseline for assessment of target characteristics.

- The resonant components for the west (copolarized) and horizontal (inclined 45° to plane of polarization) dipoles in Image 1 do not immediately reach a maximum amplitude followed by a strict decay, but require about a half cycle to reach the maximum (followed by strict decay). This could be attributed to continued coupling of remnants of the radiated pulse (see fig. 2). Another possible explanation arises from the difference in arrival time of backscattered returns from points on the targets that are at different ranges from the antenna [17].

- The 125- and 875-MHz components do not decay as quickly as expected. This phenomenon is believed to be caused by coupling of radiated-pulse remnants and/or nonlinear frequency-dependent $Q$-factors.

- The initial amplitudes of the resonant components of the dipole were not observed to scale as $1/n^2$, but scaled closely to $1/n$ (the 875-MHz component scaled more closely to prediction). Some of this behavior can be attributed to $Q$-factor variance among the components.

- The responses of the vertical (45°-inclined) and east (cross-polarized) dipoles are more anomalous; coupling may account for some of the behavior, as may relative polarization and multipath. (Apparent relative symmetry of the vertical and horizontal dipoles may not be significant because of multipath effects.)

These effects were taken into account in the target-modeling process (see sect. 3.2.4).

### 3.2.4 Determination of Variables

The variables employed in the target-modeling process for the dipoles were resonance points (real poles), initial amplitudes and decay rates of the individual resonances, and phase angles for each resonance. These variables can be categorized into three general groups: deterministic quantities (those that should follow directly from prediction), quasi-deterministic quantities (those whose general behavior is predictable, but whose specific behaviors may depend upon target characteristics, such as $Q$-factors of different resonances—these values are determined by observation), and observation-driven quantities (those for which there are no deterministic or quasi-deterministic predictors—herein referred to as "independent" variables).

Since there was only one 166.4-cm dipole available in the imagery processed, it was not considered reasonable to optimize the template variables to the empirical data for the single target and subsequently declare a recognition. Hence, the 166.4-cm dipole was employed solely to establish the baseline performance of a template generated strictly from prediction, with no optimization for observation of the actual characteristics. (Additionally, the cross-polar nature of the target renders it an unreliable measure of the target characteristics that we would expect to observe in general.)

#### 3.2.4.1 Deterministic Quantities

The quantities that should have the best prediction-observation correlation are the resonant frequencies of the targets (eq (25)). These are governed solely by the electrical lengths of the objects, and should not be observed to deviate from prediction more than a small amount allowable for minor measurement errors and other effects. These quantities did, in fact, agree very closely with the predicted values for the 114.3-cm dipole, as shown in table 1.

Table 1. Predicted and actual values of dipole resonances.

| Dipole length (cm) | Dipole resonances (MHz) | | | | | | | | | | | |
|---|---|---|---|---|---|---|---|---|---|---|---|---|
| | Harmonic 1 | | Harmonic 2 | | Harmonic 3 | | Harmonic 4 | | Harmonic 5 | | Harmonic 6 | |
| | Pred | Obs | Pred | Obs | Pred | Obs | Pred | Obs | Pred | Obs | Pred | Obs |
| 114.3 | 124 | 124 | 372 | 375 | 620 | 630 | 868 | 875 | — | — | — | — |
| 166.4 | 85 | — | 225 | — | 415 | — | 585 | — | 745 | — | 905 | — |

### 3.2.4.2 Quasi-Deterministic Quantities

Initial amplitudes and decay rates of individual components should follow equation (5), where the initial amplitude is predicted to scale as $1/n^2$ [16], and the rate of decay should be linearly proportional to frequency of oscillation [3]. Deviations from prediction will be due to the relative $Q$-factors of the dipoles at each of the harmonic components ($Q$-factor deviations will largely be determined by imperfections in the surfaces of the targets: significant surface irregularities, inhomogeneity of the constituents, etc), and are expected to be moderate, at most. Actual data did not follow the inverse-quadratic prediction exactly; a logarithmic fit to the data in table 2 suggested a fit closer to $n^{-1.78}$. Decay rates scaled closely to $n^{2.8}$ for the 125-, 375-, and 625-MHz components; the 875-MHz resonance did not follow this pattern, as shown in table 3. In both cases—amplitude and decay—the values selected in the target-modeling process were based on the empirical observations.

**Table 2. Predicted and actual values of component initial amplitudes (relative to highest frequency component).**

| Dipole length (cm) | Dipole resonances (MHz) | | | | | | | | | | | |
|---|---|---|---|---|---|---|---|---|---|---|---|---|
| | Harmonic 1 | | Harmonic 2 | | Harmonic 3 | | Harmonic 4 | | Harmonic 5 | | Harmonic 6 | |
| | Pred | Obs | Pred | Obs | Pred | Obs | Pred | Obs | Pred | Obs | Pred | Obs |
| 114.3 | 16 | 12 | 9 | 6 | 4 | 3.8 | 1 | 1 | — | — | — | — |
| 166.4 | 36 | — | 25 | — | 16 | — | 9 | — | 4 | — | 1 | — |

**Table 3. Predicted and actual values of component decay rates (relative to lowest-frequency component).**

| Dipole length (cm) | Dipole resonances (MHz) | | | | | | | | | | | |
|---|---|---|---|---|---|---|---|---|---|---|---|---|
| | Harmonic 1 | | Harmonic 2 | | Harmonic 3 | | Harmonic 4 | | Harmonic 5 | | Harmonic 6 | |
| | Pred | Obs | Pred | Obs | Pred | Obs | Pred | Obs | Pred | Obs | Pred | Obs |
| 114.3 | 1 | 1 | 2 | 7.47 | 3 | 19.18 | 4 | 7.75 | — | — | — | — |
| 166.4 | 1 | — | 2 | — | 3 | — | 4 | — | 5 | — | 6 | — |

### 3.2.4.3 Independent Variables

There was no resolvable prediction for the relative phase angles of the individual components; these were determined entirely from empirical data. Actual phase angles used represent sufficient fits to the empirical data, but are not optimized to the data. A close—but sub-optimal—fit to the data requires the detection method to have some immunity to the relative phase of the components. This is desirable since relative phase is path-length dependent; thus, it is position-dependent in the image. Although the path lengths and associated phasor corrections for each target in the image can be calculated at each resonance point, this requires substantial processing.

Ideally, we would like the recognition algorithm to perform well, independent of the wavelength (and, hence, relative phase) of the component; to achieve this goal, I use one-time, sub-optimal relative-phase corrections made during construction of the target template (no phase corrections were made for the 166.4-cm dipole). Relative phase angles employed are shown in table 4.

Table 4. Phase angles of resonant components (in degrees).

| Dipole length (cm) | Phase angle (°) | | | | | |
|---|---|---|---|---|---|---|
| | Harmonic 1 | Harmonic 2 | Harmonic 3 | Harmonic 4 | Harmonic 5 | Harmonic 6 |
| 114.3 | -10 | 180 | 60 | -90 | — | — |
| 166.4 | 0 | 0 | 0 | 0 | 0 | 0 |

## 3.3 Construction of Target Templates

Based on the observations in section 3.2, target templates were constructed to provide models of the resonant responses of the dipoles. Linearity of the resonance effects was assumed in the modeling process, so the templates were constructed by simple superposition of the individual component ringdowns. Each component was defined by four parameters: frequency of oscillation, amplitude, damping factor, and phase. The ringdown for each component was constructed at the effective sampling rate of the focused image (3994 MHz) by the use of

$$R_n[i] = A_n \sin(\Theta_i)e^{-i\xi_n}\sin\left[\frac{\omega_n}{\omega_s} i + \varphi_n\right] , \qquad (26)$$

where

$$\Theta_i = \begin{cases} \theta_i & \text{for } \theta_i \leq \frac{\pi}{2} \\ \frac{\pi}{2} & \text{elsewhere} \end{cases}, \qquad \theta_i = \left(\frac{\pi}{2} i\right)\left(\frac{\omega_n}{\omega_s} + 1.5\right), \qquad (27)$$

the index $n$ is the component number, and the index $i$ equates to the pixel position in the ringdown (i.e., the amplitude of the response of the third harmonic component at pixel position 9 in range is defined by $R_3$ [9]). In both equations, $\omega_n$ is the oscillation frequency of the $n^{th}$ harmonic component and $\omega_s$ is the effective sampling frequency in radians; $A_n$, $\xi_n$, and $\varphi_n$ are, respectively, the initial amplitude, decay rate, and phase angle for each component. Equation (27) governs the "growth" factor (the first sine term in eq (26)) during the first half-cycle of the response; the effect of this term is removed after the first half-cycle by the definition of $\Theta_i$ in equation (27).

38

Using equation (26) to define the individual harmonic components, I constructed the combined response straightforwardly as a linear sum of the $N$ components:

$$R_{target_k}[i] = \sum_{j=1}^{N} R_j[i] , \quad k \in \{\text{target set}\} . \tag{28}$$

Figure 18 shows the combined responses (herein referred to as "synthetic ringdowns") for the 114.3- and 166.4-cm dipole. In this figure, the modeling of the half-cycle growth phenomenon is clearly visible.

## 3.4 Development of Target-Recognition Methodology

Each image to be processed contains at least one dipole target; the ringdowns from these dipoles will appear in range pixels "behind" the targets (see app A). I employ Fourier and multiresolution techniques to extract the spectral information from the resonant signatures; the data obtained can then be correlated with the spectral characteristics of the target templates, yielding a scalar correlation coefficient. This approach lends itself to establishment of a single target-declaration threshold, which—if exceeded—will result in a

**Figure 18. Synthetic ringdowns: (a) 114.3-cm dipole and (b) 166.4-cm dipole.**

(a)



(b)
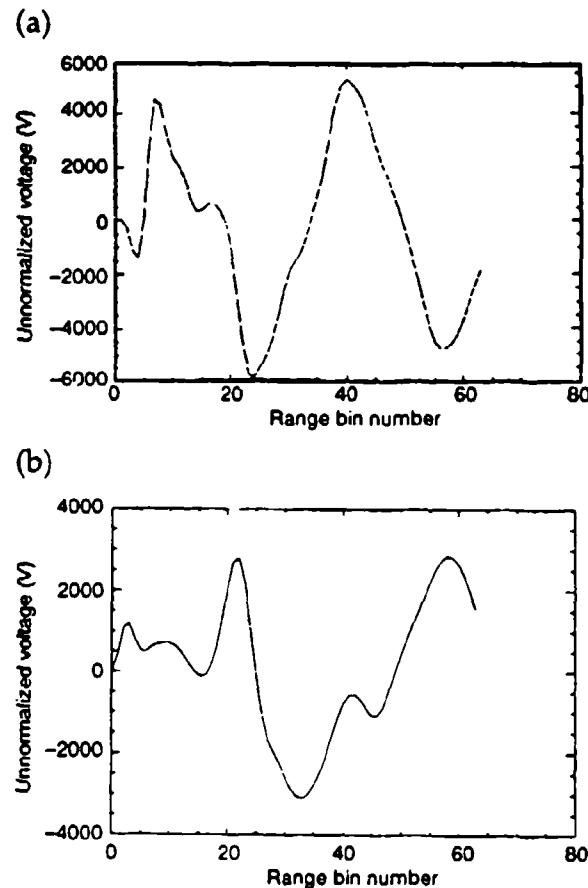
target declaration. This information will not guarantee that the declared target exists at that location—the declaration may be a false alarm—but it can be passed to another system for further analysis. Thus, some set of goals and criteria must be established for the performance of the target-recognition processor to be evaluated.

### 3.4.1 Target-Recognition Criteria

The long-range ATR system envisioned for the UWB system currently centers on a neural-network-based processor. Since short-term projections of throughput rates for neural nets are not high enough to provide realistically fast response times, the ATR architecture will require a preprocessor to provide target "cues" to the net, thereby reducing its processing load. The goal of this research is to provide a preprocessor that will have a very high target-recognition probability (0.90 or higher), with a relatively low false-a'- -n rate (0.001 or fewer false alarms per pixel processed). Thus, _ _ll- deavor to ensure that the vast majority of real targets in the processed images are presented to the neural net, while reducing the throughput requirements of the net by about three orders of magnitude.

The requirement to recognize a fairly high percentage of targets presented to the processor is significant: targets at sub-optimal orientations (i.e., orientations that place key resonators within shadows) will yield severely attenuated or otherwise modified signatures. Meeting this criterion requires the recognition processor to exhibit a high degree of immunity to degradation of the target-signature characteristics. Since this is not a trivial requirement, I concentrate in this work on targets at orientations considered sub-optimal (for dipoles, sub-optimal orientations are those in which the major axis of the dipole lies outside the image plane of polarization). Optimal orientations were used in the construction of the template for the 114.3-cm dipole, since the high RCS inherent in those orientations provides the strongest signal return, and thus the best characterizations of the target. The goal, however, is for these templates to meet the recognition requirements, which include declaration of all targets—at all orientations—in the images.

### 3.4.2 Spectral-Analysis Approach

The recognition approach is based on transformation of the target data into the frequency domain, and correlation of the spectral characteristics with those of the "known" target (template). Thresholding the scalar correlation coefficient provides a computationally efficient means of determining target declarations.

The scalar correlation approach also provides a mechanism for detection of targets with very weak signatures: since the method hinges on finding relative symmetry between the two sets of spectral coefficients—not on matching their actual magnitudes—it features considerable immunity to target signature attenuation. This obviates the requirement to scale the template to the suspected magnitude of the data (as must be done, for example, in FLIR imagery to account for range-related target scalings, and in radar systems using pattern-based algorithms, to accommodate modulations in target intensity).

### 3.4.2.1 Determination of Analysis Window

For consistency of comparison among the various transform methods employed, identical-length analysis windows were employed in all analyses. Since the FFT analysis window length is, for all intents and purposes, constrained to integer powers of 2, the range of possible window sizes was limited to those values.

Empirical observations of the data were used to establish the length of the window. Analysis of the range-line cut from the response of the west dipole in Image 1 (fig. 19) shows the driven response (boxed area) with the ringdown commencing shortly thereafter. (Note that pixel numbers in range-line illustrations indicate relative positions, not absolute positions, in the range line; furthermore, different polarizations of the same image are currently unregistered, so their pixel coordinates do not align.) According to prediction, all components of the ringdown will decay within a similar number of cycles; thus, the total time required for the response to ring down to half power will be dictated by the lowest frequency (i.e., longest wavelength) component. For the 114.3-cm dipole, it is the 125-MHz

Figure 19. Driven response (boxed area) and resonant response of west dipole in Image 1. Numbers indicate relative pixel positions in ringdown portion of response.



Relative range bin number (range line 1123, pixel 1130)

41
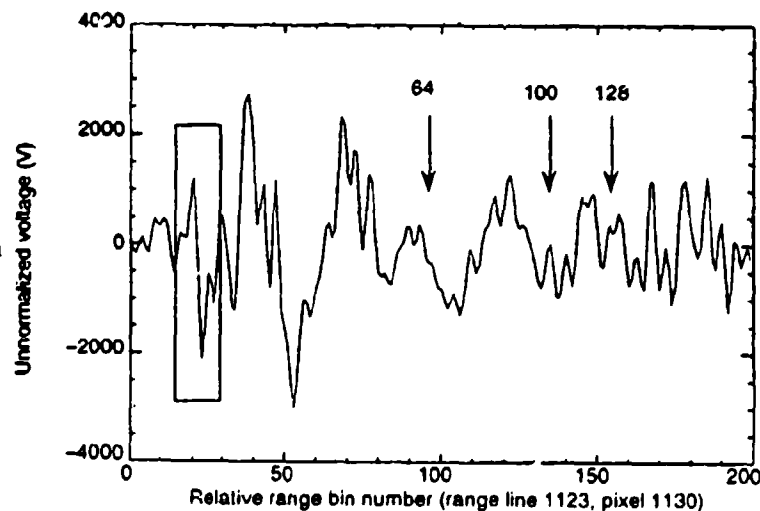
component that will determine the decay time—which requires about 100 pixels before the signal has decayed into the noise. Employing a 128-point analysis window would thus reduce the S/N ratio of the transformed data, suggesting that a 64-point window should provide the best—albeit sub-optimal—performance (these points are identified in the ringdown portion of the west-dipole response shown in fig. 19). This assumption was also borne out by experiment: the 128-point window performed poorly compared to the 64-point window.

For comparison, the west dipole ringdown and the dipole template are juxtaposed in figure 20. Note that the two sequences are not closely correlated (their correlation, in fact, is about 0.62). It will be shown that an exact match of the template with the data is unneces-

(a)

Figure 20. Comparison of (a) west-dipole ringdown and (b) synthetic ringdown template (114.3-cm dipole).



(b)
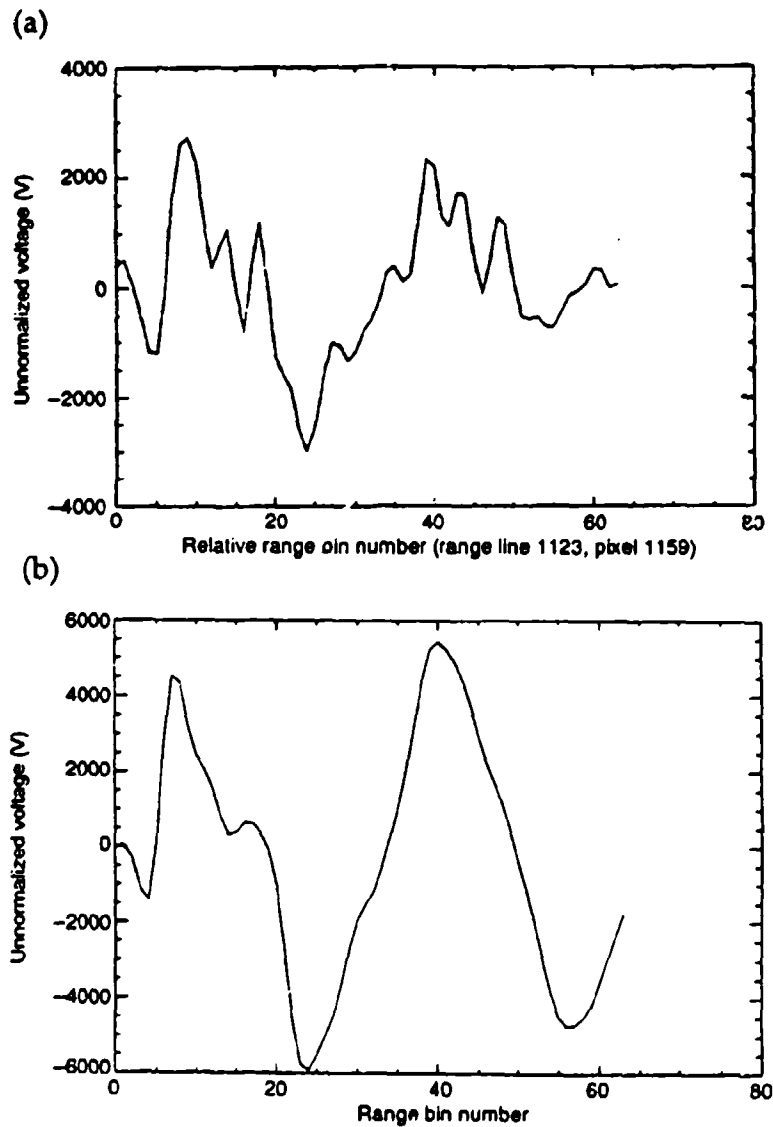
sary—the key is that their spectra correlate sufficiently well to provide adequate detectability of the targets.

### 3.4.2.2 Analysis Bases Employed

Six analysis bases were evaluated in the course of this research, although only four of them performed sufficiently well to warrant detailed inclusion here. Of the four bases evaluated in detail, two are Fourier bases (rectangular- and Gaussian-windowed FFTs) and two are multiresolution bases (the Haar wavelet and the Gaussian basis). The other two bases—which are not included in the detailed analysis—are the first-order Gaussian derivative and difference-of-Gaussian multiresolution bases.

*Fourier bases.* A standard rectangular-windowed FFT was employed in the Fourier analysis. I also evaluated the Gabor basis (a Gaussian-weighted FFT), both to reduce rectangular-window-related ringing and to provide a basis for comparison with the Gaussian multiresolution basis. (Sect. 2.4.2.2 gives a brief discussion of the Gabor basis.) Target-recognition performance was similar for both the square-windowed FFT and the Gabor basis, although the Gabor basis had substantially higher false-alarm rates (despite the fact that the Gabor basis exhibited greater detectability of the targets, thereby permitting a higher target-declaration threshold to be established).

The performance characteristics of both bases are summarized and analyzed in section 3.5; the detailed results are tabulated in appendix C.

*Primary multiresolution bases.* Unlike Fourier methods, there is a plethora of multiresolution and wavelet bases available. Although several bases were investigated, I summarize only two: the Haar basis,

$$W_{m,k}(t) = W(2^m t - k), \quad m \geq 0, \quad 0 \leq k < 2^m, \quad m, k \in Z , \qquad (29)$$

and the Gaussian basis,

$$W_{m,k}(t) = \frac{1}{\sqrt{2\pi}} \exp\left[-\frac{\left(2^m t - k\right)^2}{2}\right], \quad m \geq 0, \quad 0 \leq k < 2^m, \quad m, k \in Z . \quad (30)$$

The Haar basis—which provided relatively good performance—is piecewise continuous; thus, it introduces ringing effects, and does not provide very good correlation with the sinusoids being analyzed.

The desire for improved performance with sinusoids motivated the introduction of the Gaussian basis. Although the Gaussian does not satisfy the requirements to be considered a wavelet basis in the strict sense (square-integrability and true compact support), it is nevertheless employed here for its ability to provide satisfactory correlation with sinusoids.

Each basis used a 64-point analysis window (referred to as the "primary window" in multiresolution analysis, since the window sizes scale in inverse-dyadic style as the analysis scale decreases); the shortest windows employed were two-point windows for the Haar and four-point windows for the Gaussian. (The piecewise-constant Haar basis reduces to two points in a straightforward manner; the Gaussian does not.) This yields a 64-vector spanning set in the Haar case, and a 31-vector basis in the Gaussian case.

The Haar basis is illustrated in figures 12 and 13; the Gaussian function is shown in figure 21.

*Other multiresolution bases employed in the analysis.* Two other bases were also employed in the analysis—a first-order Gaussian derivative (FOGD) function,

$$W_{m,k}(t) = \frac{1}{\sqrt{2\pi}} \exp\left[-\frac{(2^m t - k)^2}{2}\right], \quad m \geq 0, \quad 0 \leq k < 2^m, \quad m, k \in Z, \tag{31}$$

and a difference-of-Gaussian (DOG) function,

$$W_{m,k}(t) = \frac{2\pi^{1/4}}{\sqrt{2\pi}} \left[1 - (2^m t - k)^2\right] \exp\left[-\frac{(2^m t - k)^2}{2}\right], \quad \left\{ \begin{array}{l} m \geq 0, \\ 0 \leq k < 2^m \end{array} \right\}, \quad m, k \in Z. \tag{32}$$

Although these bases satisfy the square-integrability condition for wavelet bases, they do not have compact support, nor do they provide orthogonal projections. (Orthogonality is unnecessary in this application, since the transform is performed in only one direction.)

Similar to the Gaussian basis, these bases were introduced for their sinusoidal correlation characteristics. These functions, however, are difference operators, and correlate well with wideband, impulsive data. Since the clutter in the UWB SAR imagery has largely impulsive characteristics, these bases yielded very high false-alarm rates, and were not employed in the analysis summarized in section 3.5.

The FOGD and DOG basic wavelets are shown in figure 22.

**Figure 21. The Gaussian basic wavelet.**
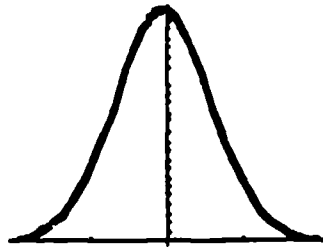
**Figure 22. Wavelet basis functions: (a) first-order Gaussian derivative (FOGD), and (b) difference of Gaussian (DOG).**

(a)                          (b)
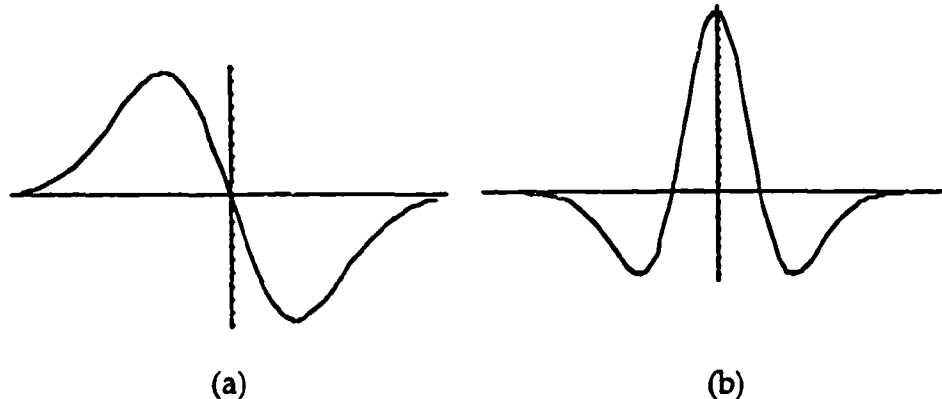
### 3.4.2.3 Construction of Spectral Templates

I generated the target templates by transforming the synthetic ringdowns to generate a set of spectral coefficients (the "spectral template"). The FFT bases each yielded 33 unique complex coefficients (the other 31 are just conjugate-symmetric projections of the 31 poles that lie entirely in the upper half of the complex plane; see sect. 2.4.2.2), the Haar basis yielded 64 coefficients, and the Gaussian basis yielded 31 coefficients; all values are tabulated in appendix B.

### 3.4.2.4 The Recognition Process

To provide the best possible characterization of the target-recognition performance, the processor performed the transforms on *every* pixel in the target area; i.e., the 64-point analysis window was incremented by one pixel for each transformation. The transforms were performed in range only. Each transform yielded a set of spectral coefficients, which was correlated with the corresponding spectral template to produce a correlation coefficient. This coefficient characterized the confidence that the target of interest was present in the transformed data.

45

To establish the thresholds employed in the target-declaration process, I transformed and characterized the data in Image 1 for each of the four targets present in the image; these characterizations are tabulated in appendix C. Because we wish to recognize every target in the image, the thresholds were derived from the minimum correlation values across the target set. The results of this process are summarized in section 3.5.

*Hardware and software resources employed.* The hardware platform employed in the analysis was a Sun Corporation VME-based Sparc 1 processor. Four CSPI i860-based vector processors were also employed at later stages in the analysis.

Most of the code was written in the PV-WAVE command language (Precision Visuals, Inc.). Software for CSPI processors was written in the "C" programming language.

*Processing-time considerations.* Each image analyzed contains 8 megapixels on a Cartesian grid, with 4096 pixels in range and 2048 pixels in azimuth. To perform a 64-point transform at every pixel in range (4032 transformations) for a single range line requires roughly 3 minutes of processing time on an unloaded processor; hence, 2048 range lines would require 102.4 hours (4.25 days) of processing time. Considering the 80 hours required to collect an aperture, this can still be considered near-real time; it is, however, unreasonable from a practical standpoint. Processing-time considerations thus motivated the development of some form of target cueing to reduce the number of transformations required to analyze an image.

*Target cueing.* The driven response of the target provides an excellent detection mechanism for provision of target cues to the recognition processor; this response has a duration of about 20 pixels for a target of short dimension in range, and precedes the resonant response by 5 to 10 pixels (see boxed area in fig. 19). The magnitude of the response is not necessarily greater than that of the ringdown; in fact, it may be substantially less—an interesting characteristic discussed elsewhere [15]. Nevertheless, an acceptable target detector can be employed that uses the driven response of the target to cue the recognition engine.

Since the topic of this report is the recognition of targets by their resonant responses, I describe the nature of the detection algorithm only briefly.

To avoid a speed penalty, I used only a single transform method in the detection stage. Between the Haar basis and the Fourier basis, it was found that a 16-point Haar wavelet provided better detection

performance in terms of reliability in recognizing the presence of targets and in rejecting false cues. The detector provided an average of 36,000 discrete detections per image, resulting in a substantial decrease in processing time. Note that each target will span several pixels in azimuth, each one providing at least one detection. Thus, the detections can be clustered into target groupings, representing about an order of magnitude decrease in detections. This optimization, however, was not employed, since the larger number of detections provided a better statistical characterization of the recognition algorithm's performance.

The ringdown appears in pixels in range behind the driven response; however, the "distance" between the start of the driven response and the start of the ringdown is variable, spanning about 15 pixels. Thus, the recognition algorithm spanned 20 pixels in range (including a 5-pixel safety buffer) following each target cue provided by the detector. For an average of 36,000 detections per image, this resulted in about 720,000 transformations being performed for each transform method employed, or slightly better than an order-of-magnitude improvement over the full-image-decomposition approach.

When the Haar-based cueing mechanism was used, the processing time required to analyze a single image was reduced from 102 hours to about 7 hours (per transform method employed)—a substantial improvement.

It is worth noting that there was no significant correlation between the detection technique employed (Fourier, Haar, and Gauss) and the recognition performance among the transform methods; that is, using Fourier detections did not improve the performance of the Fourier-based recognizer. (In fact, the Fourier false-alarm rate tended to increase slightly when the Fourier-based detector was used, with no corresponding increase in recognition performance.)

### 3.4.2.5 Basis Pruning

Since the ringdown components appear in only a few of the spectral coefficients for each transform method, not all the coefficients are required for the target to be detected. This motivates some "pruning" of the basis to remove those coefficients that do not contribute to the recognition process. Care must be taken in this process, however, since random-noise correlations begin to increase the false-alarm rate as spectral coefficients are removed from the correlation process. This suggests that there must exist some optimal set of basis functions; no claim is made that the basis pruning employed here was optimal. It did, however, increase recognition performance and

decrease false-alarm rates for each transform method. Decreases in false-alarm rates of pruned bases resulted from the increased declaration thresholds permitted by the semi-optimized transforms.

Note that pruning de-orthogonalizes the basis (the Gaussian basis, as discussed in sect. 3.4.2.2, is not an orthogonal basis from the outset), which limits the reconstructability of the original data. Since the transform is performed in only one direction for the purpose of target recognition, reconstructability of the original data is not an issue. (Additionally, the transforms were not performed in place, so the original data were not lost in the process.)

The method of pruning was straightforward: basis functions that resulted in a significant (greater than 1 percent) decrease in correlation performance were removed from the basis. This process is briefly described for each basis; spectral coefficients are tabulated in appendix B.

The Fourier basis was especially sensitive to increased false alarms with basis pruning; in fact, only one of the 33 complex coefficients was removed from the basis. Removal of other coefficients did not result in a significant increase in detectability, but did significantly increase false-alarm rates. The basis removed corresponded to the highest frequency subband; at the effective sampling rate (3994 GHz), this is about a 2-GHz basis function. Since there are no data above approximately 1 GHz, this subband is clearly unnecessary. (By the same reasoning, about half of the basis functions could be eliminated. While any one of them provided roughly the same improvement in performance, removing more than one resulted in a steadily increasing false-alarm rate. The one selected for removal had the most significant impact on the recognition performance.)

The Gabor basis was pruned in the same manner as the square-windowed FFT basis, permitting direct performance comparisons between the two bases. As suggested by the analyses in sections 3.5.1 and 3.5.2, the Gabor basis may lend itself to more extensive pruning than the rectangular-windowed FFT because of the Gaussian-window suppression of the high-frequency ringing.

The Haar basis exhibited the poorest performance for a complete basis (see table 5, sect. 3.5.1), and also tolerated the most extensive pruning. The basis was reduced from 64 to 36 vectors, and even reductions down to 26 vectors did not yield intolerable false-alarm performance. The basis functions removed were generally those that transformed "empty" subbands (those without resonances) or transformed ringdown components before initiation or after they had de-

cayed into noise. The pruned basis yielded greater target-recognition performance with substantially decreased false-alarm rates.

The Gaussian basis exhibited the best full-basis performance, and hence benefited from only minimal pruning. Similar to the Fourier case, the Gaussian basis was more sensitive to increases in false-alarm rates as more basis vectors were removed. Only two vectors were removed from the Gaussian basis, corresponding to scale/translation combinations in which there were no ringdown contributions.

## 3.5 Performance Summary

A summary and analysis of the recognition performance are provided here; detailed results are tabulated in appendix C.

I ran an initial transform on Image 1 using complete bases to establish baseline performance of the transform methods. The bases were then pruned to semi-optimal states; the pruned bases were employed in all subsequent analyses.

### 3.5.1 Image 1: Run 1, WW Polarization (Complete Bases)

The baseline transform was performed on Image 1, since it is a copolarized image containing all four dipole orientations. Figure 23 is an image chip containing all four dipoles, identified by the boxes. The dipoles are enlarged to show greater detail in figure 24; the resonant ringdown is clearly visible in range pixels behind the centroid of the west dipole's driven response (at the bottom of fig. 24c). Also notable is the weak response from the east (cross-polarized) dipole; the great majority of brighter pixels in this image chip are clutter cells. This is also clear from examination of the range profiles (fig. 25).

The first four data columns in table 5 show the correlation performance of the bases; note that the Haar basis exhibited very poor target-recognition performance in this case. Based on these data,



Figure 23. Run 1, WW image chip, showing dipole ringdowns (from L to R: vertical, east, west, and horizontal dipoles). Bright area at top center of image is a corner reflector (40 dBsm at 1 GHz).

49

**Figure 24. Enlarged image chips, Image 1 dipoles: (a) vertical, (b) east, (c) west, and (d) horizontal.**



(a)  (b)  (c)  (d)

(a)



(b)



(c)



(d)



Figure 25. Range profiless, Image 1: (a) vertical dipole, (b) east dipole, (c) west dipole, and (d) horizontal dipole.

50

**Table 5. Recognition performance, Image 1, complete bases.**

| Transform method | Target correlation coefficients by dipole orientation | | | | Thresh-old | No. false alarms |
|---|---|---|---|---|---|---|
| | Vertical | East | West | Horizontal | | |
| FFT | 0.592 | 0.514 | 0.719 | 0.811 | 0.50 | 8,855 |
| Gabor | 0.629 | 0.610 | 0.825 | 0.887 | 0.60 | 51,636 |
| Haar | 0.348 | 0.304 | 0.357 | 0.371 | 0.30 | 63,527 |
| Gaussian | 0.872 | 0.801 | 0.927 | 0.912 | 0.80 | 1,056 |

target-declaration thresholds were established, and I ran the transforms on the entire image to obtain false-alarm-rate information; thresholds and associated false-alarm rates are shown in the last two columns of the table. Again, the Haar basis performed very poorly. The Gabor basis also exhibited poor false-alarm performance for the complete basis. Analysis of the spectral coefficients (app B) reveals that the high-frequency ringing introduced by the rectangular window of the FFT is largely suppressed in the Gabor case, as expected; this suppression, however, yields a higher false-alarm rate because of the corresponding increase in correlation values driven—in part—by similar suppression of ringing in the analyzed data. The FFT performed acceptably in this case, although the false-alarm rate is slightly higher across the 8-Mpixel image than the goal of $10^{-3}$. The performance of the Gaussian basis was encouraging—for both target detectability and false-alarm rate—despite the lack of basis optimization.

### 3.5.2 Image 1: Run 1, WW Polarization (Pruned Bases)

I ran the analysis once again on Image 1 following the basis-pruning step, to obtain a comparison with the unpruned bases. Again, the first four data columns (table 6) summarize the correlation performance, and the last two columns show the selected false-alarm thresholds and associated false-alarm rates. In both of these cases (Image 1, unpruned and pruned), the thresholds were established at levels that ensured recognition of all targets.

Note that the pruned Haar basis has realized a substantial increase in performance, in terms of both correlation performance (which al-

**Table 6. Recognition performance, Image 1, pruned bases.**

| Transform method | Target correlation coefficients by dipole orientation | | | | Thresh-old | No. false alarms |
|---|---|---|---|---|---|---|
| | Vertical | East | West | Horizontal | | |
| FFT | 0.658 | 0.606 | 0.808 | 0.922 | 0.60 | 8,709 |
| Gabor | 0.699 | 0.668 | 0.947 | 0.985 | 0.66 | 18,131 |
| Haar | 0.759 | 0.627 | 0.853 | 0.921 | 0.60 | 4,845 |
| Gaussian | 0.904 | 0.840 | 0.915 | 0.977 | 0.80 | 1,146 |

51

lowed the declaration threshold to be raised significantly) and false-alarm rate. Performance improvements were also realized for both the Fourier and Gaussian bases. In the Gabor case, the false-alarm rate remained high, despite the increase in the target-declaration threshold; improved basis pruning may yield increased performance for this basis.

### 3.5.3 Image 2: Run 1, EW Polarization

Image 2 is the east-west-polarized image from the first aperture run. In this and subsequent analyses, I held the stated target-declaration thresholds constant to provide a basis for performance comparisons among the images analyzed (I show constant declaration thresholds in **bold** to underscore this fact). In this case, the Gaussian multiresolution basis and both of the Fourier bases failed to recognize the vertical target (table 7). One option in this event was to lower the target-declaration threshold, and re-evaluate the performance. This option, however, resulted in an unacceptably high number of false alarms in the analysis; thus, accepting the target "misses" was considered the better option.

The Gabor basis exhibited a substantially higher false-alarm rate for this image; there is currently no explanation for this behavior.

Not surprisingly, the recognition performance for the east dipole improved significantly across all bases for this image polarization; analysis of the range-line profile for the east dipole indicates a substantially "cleaner" signature for this image. Range profiles for all targets in Image 2 are shown in figure 26.

**Table 7. Recognition performance, Image 2.**

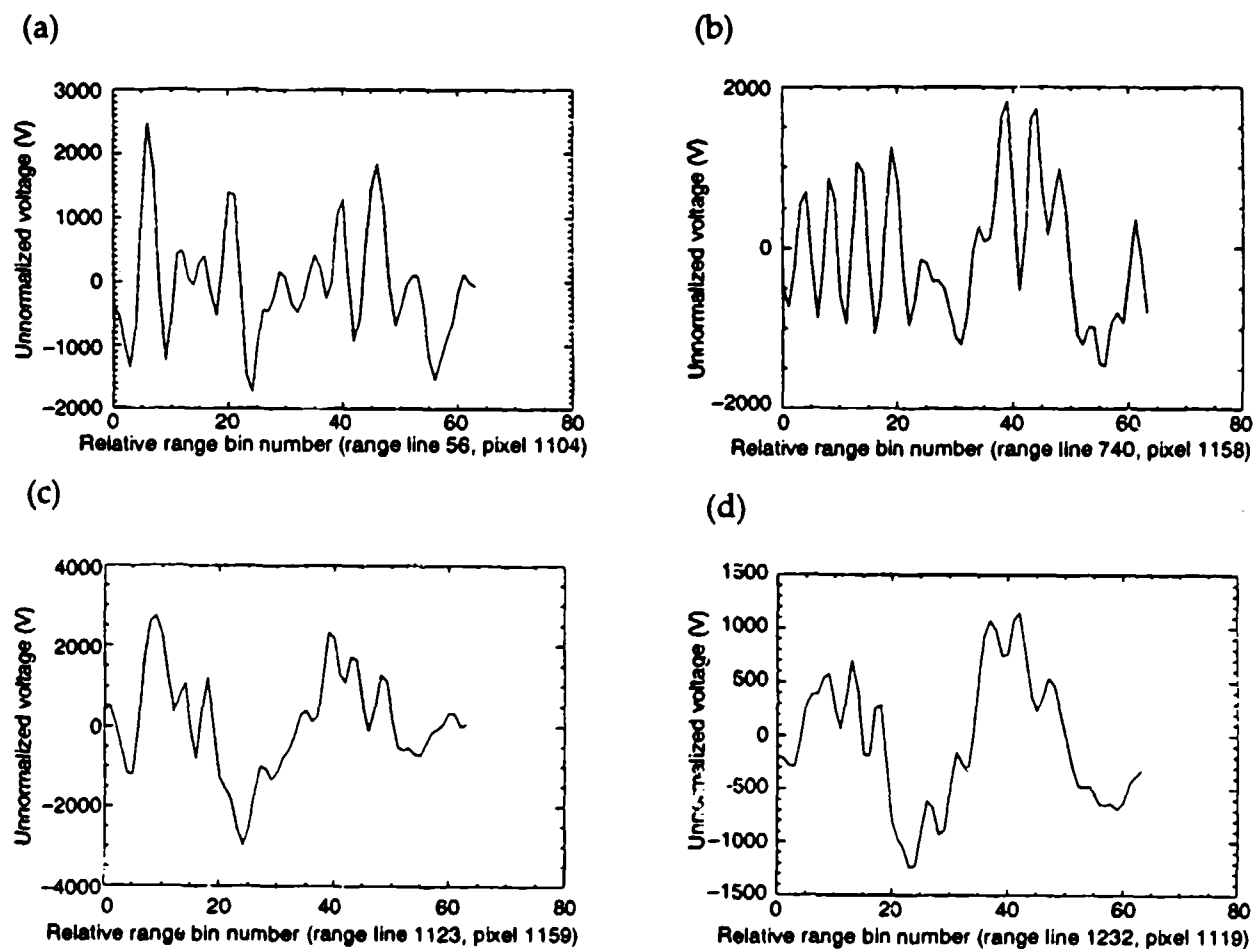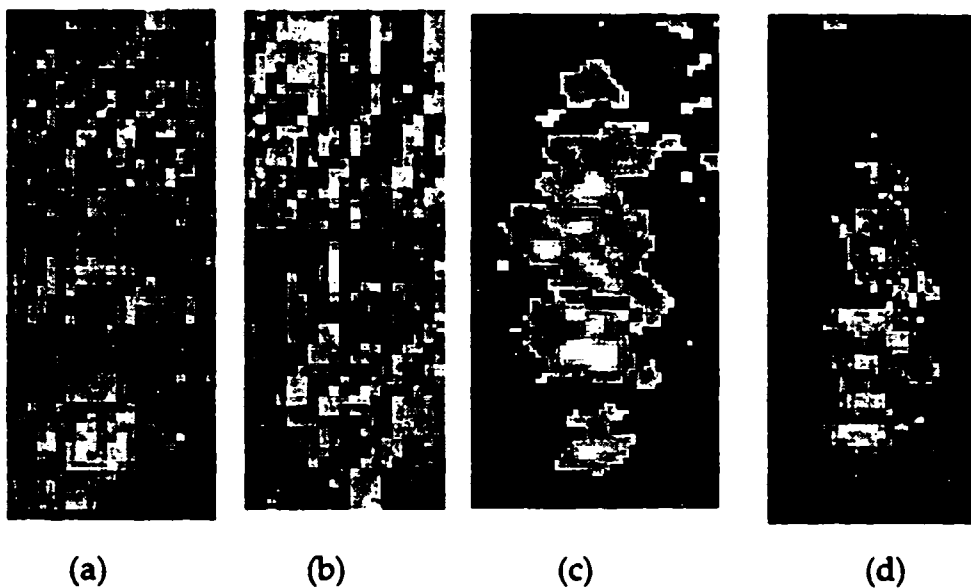| Transform method | Target correlation coefficients by dipole orientation | | | | Thresh-old | No. false alarms |
|---|---|---|---|---|---|---|
| | Vertical | East | West | Horizontal | | |
| FFT | X | 0.698 | 0.784 | 0.845 | 0.60 | 8,020 |
| Gabor | X | 0.822 | 0.889 | 0.894 | 0.66 | 35,748 |
| Haar | 0.663 | 0.728 | 0.810 | 0.812 | 0.60 | 3,973 |
| Gaussian | X | 0.863 | 0.939 | 0.925 | 0.80 | 1,172 |

X = not recognized.

**Figure 26. Range profiles, Image 2: (a) vertical dipole, (b) east dipole, (c) west dipole, and (d) horizontal dipole.**

### 3.5.4  Image 3: Run 4, WW Polarization

Image 3 is the west-west polarization state from the fourth aperture run. One target is present in the image, oriented up east (cross-polarized to image polarization plane); its range profile is shown in figure 27. In this image, the Haar wavelet failed to recognize the target (table 8); similar to the previous case, an unacceptably high number of false alarms resulted when the target-declaration threshold was decreased to the point at which the target was admitted.

### 3.5.5  Image 4: Run 6, WW Polarization

Image 4 is the west-west polarization state from the sixth aperture run. One target is present in the image, oriented up east; the range profile for this target is shown in figure 28. Once again, the Fourier bases failed to recognize the target (table 9). Haar and Gaussian bases displayed acceptable performance, although false alarms have increased in this image (possibly due to the presence of a greater number of unrelated targets in the image).

**Figure 27. Range profile, east dipole, Image 3.**

*Unnormalized voltage (V)* vs *Relative range bin number (range line 1525, pixel 1171)*
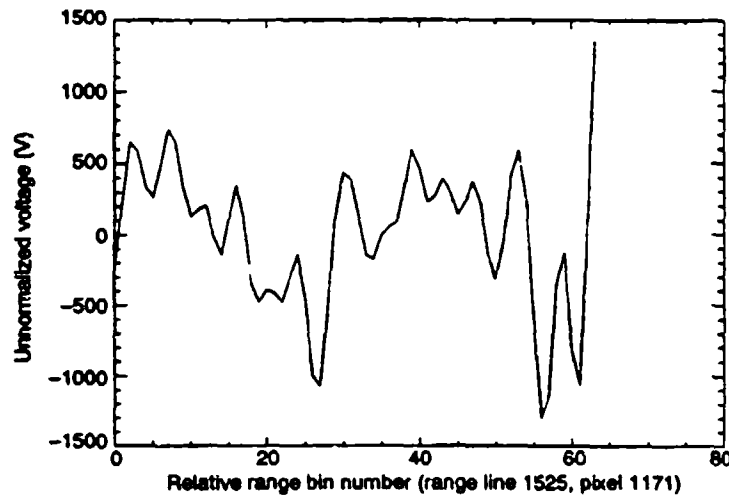
**Table 8. Recognition performance, Image 3.**

| Transform method | Target correlation coefficient for east dipole | Threshold | No. false alarms |
|---|---|---|---|
| FFT | 0.620 | 0.60 | 5,182 |
| Gabor | 0.863 | 0.66 | 12,068 |
| Haar | X | 0.60 | 2,099 |
| Gaussian | 0.925 | 0.80 | 503 |

X = not recognized.

**Figure 28. Range profile, east dipole, Image 4.**

*Unnormalized voltage (V)* vs *Relative range bin number (range line 1525, pixel 1172)*
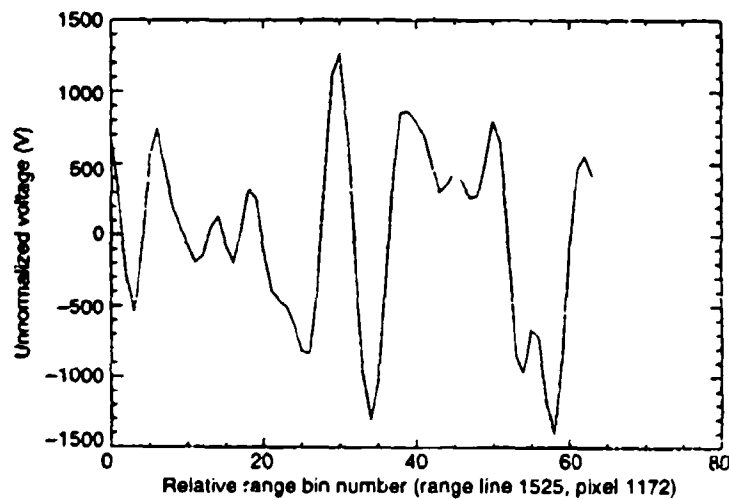
**Table 9. Recognition performance, Image 4.**

| Transform method | Target correlation coefficient for east dipole | Threshold | No. false alarms |
|---|---|---|---|
| FFT | X | 0.60 | 13,019 |
| Gabor | X | 0.66 | 29,101 |
| Haar | 0.668 | 0.60 | 7,054 |
| Gaussian | 0.846 | 0.80 | 2,601 |

X = not recognized.

### 3.5.6  *Image 5: Run 7, WW Polarization*

This image is the west-west polarization state from the seventh aperture run. Two targets are present in the image, one 114.3- and one 166.4-cm dipole, both oriented up east and embedded in foliage. Range profiles for each target are shown in figure 29. Table 10 summarizes the performance for the 114.3-cm dipole, and table 11 summarizes the 166.4-cm dipole results.

The 166.4-cm dipole was successfully recognized when unpruned (complete) bases were used with a template constructed directly from prediction, and no modifications were made to account for deviations in the data. Of course, the term "successfully" is being used somewhat loosely here, since the target thresholds were established at their absolute maximum values—solely to provide at least one target recognition in each case. The "success" of the method is based



**(a)** Unnormalized voltage (V) vs. Relative range bin number (range line 735, pixel 1415)

**(b)** Unnormalized voltage (V) vs. Relative range bin number (range line 1540, pixel 1416)
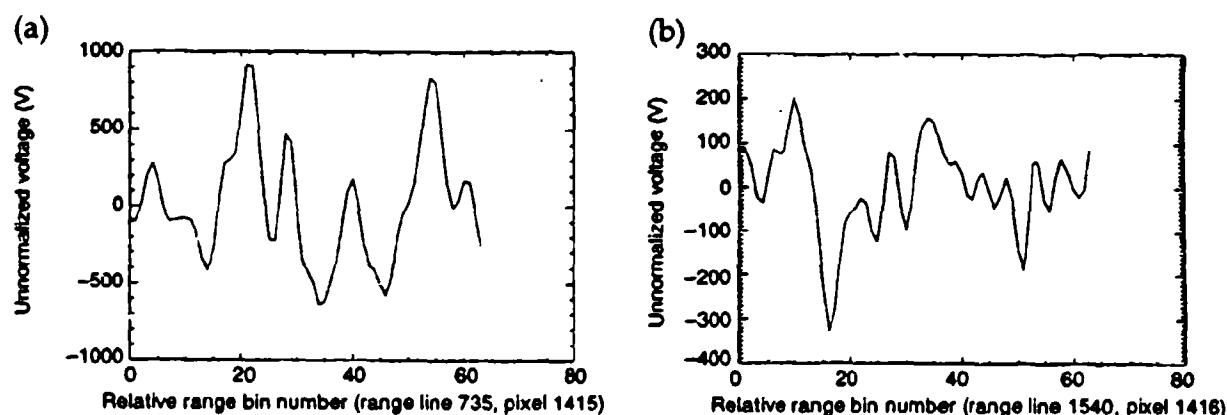
**Figure 29. Range profiles, Image 5: (a) 166.4-cm dipole and (b) 114.3-cm dipole.**

**Table 10. Recognition performance, Image 5, 114.3-cm dipole.**

| Transform method | Target correlation coefficient for east dipole | Threshold | No. false alarms |
|---|---|---|---|
| FFT | 0.603 | 0.60 | 2,964 |
| Gabor | 0.735 | 0.66 | 10,627 |
| Haar | 0.688 | 0.60 | 1,424 |
| Gaussian | 0.811 | 0.80 | 516 |

**Table 11. Recognition performance, Image 5, 166.4-cm dipole.**

| Transform method | Target correlation coefficient for east dipole | Threshold | No. false alarms |
|---|---|---|---|
| FFT | 0.573 | 0.57 | 16,280 |
| Gabor | 0.665 | 0.66 | 53,273 |
| Haar | 0.565 | 0.56 | 2,072 |
| Gaussian | 0.849 | 0.84 | 5,265 |

on the fact that this baseline evaluation provided results comparable to the baseline (unpruned basis) example for the up-east 114.3-cm dipole in Image 1 (table 5)—the Haar basis, in fact, provided substantially better performance in this baseline analysis. The Gaussian basis performed well, although it did yield a relatively high false-alarm rate; basis pruning may improve the false-alarm statistics. The Fourier bases demonstrated the poorest performance, with a false-alarm rate substantially higher for the rectangular-windowed FFT than that observed for the 114.3-cm target. The Gabor basis exhibited a complete-basis false-alarm rate similar to that demonstrated in the 114.3-cm-dipole case.

The combination of basis pruning and moderate template optimization should provide performance similar to that observed for the 114.3-cm dipole. For the Gabor basis, however, more optimization may be required before the false-alarm rate can be reduced to an acceptable level.

Note that the foliage-induced signal attenuation for the 114.3-cm dipole did not result in a significant degradation in the detectability of the target (table 10). In this example, the low operating band of the UWB radar provided penetration into the foliage with relatively moderate attenuation (about 19 dB); furthermore, the spectral-correlation scheme provided satisfactory target-recognition performance for the foliage-attenuated ringdown, as desired.

## 3.6    Performance Analysis

The goals of the analysis were to provide a recognition probability of 0.90 or better, with a false-alarm rate of 0.001 per pixel processed: by this standard, the Gaussian basis certainly provided the best performance of the bases considered in this work (table 12). Both the Haar and the Gaussian bases met the recognition goal of 90 percent; the Fourier bases each fell short of the goal by a single target recognition.

False-alarm rates were also relatively low for all bases except the Gabor wavelet: since 20 pixels were processed for every target detec-

Table 12. Performance summary.

| Transform method | Probability of recognition | No. false alarms per pixel | |
| --- | --- | --- | --- |
| | | Cues only | Entire image |
| *Goal* | 0.90 | — | $10^{-3}$ |
| FFT | 0.82 | $11 \times 10^{-3}$ | $0.4 \times 10^{-3}$ |
| Gabor | 0.82 | $146 \times 10^{-3}$ | $13 \times 10^{-3}$ |
| Haar | 0.91 | $5 \times 10^{-3}$ | $0.2 \times 10^{-3}$ |
| Gaussian | 0.91 | $2 \times 10^{-3}$ | $0.07 \times 10^{-3}$ |

tion, the goal is almost met when only recognition processing is considered. Since the detection algorithm processed every pixel in the image and provided cues to the recognition engine, we can summarize the performance of the two-stage processor as shown in the last column of table 12. These figures easily surpass the goal of 0.001 false alarms per pixel processed for the rectangular-windowed FFT and both multiresolution bases.

The Gabor basis demonstrated substantially higher false-alarm rates than the other bases. The symmetrical Gaussian weighting function employed by the Gabor basis is suppressing the early portion of the resonant signature, where the ringdown components exhibit their highest amplitudes; this may adversely affect the recognition performance of the Gabor basis, resulting in an artificially low target-declaration threshold and a correspondingly higher false-alarm rate. This suggests that a nonsymmetrical tapered window—with a decay similar to that observed for the target ringdown—may yield improved performance.

Recognition performance was similar between the two Fourier bases studied, leaving false-alarm rate as the deciding measure; by this metric, the rectangular-windowed FFT is clearly superior to the Gabor basis, although neither Fourier basis performed as well as the multiresolution bases in either false-alarm rates or recognition capabilities.

Inspection of the individual false alarms indicates that they usually occur in neighborhoods in the images, suggesting that they are generally being triggered by objects in the images and not by random noise. This is somewhat to be expected, based on the structural simplicity of the target; most objects of similar dimension in the imagery will have closely correlated spectral characteristics, thereby triggering false alarms. Further reductions in false-alarm rates should be realized for more structurally (hence, spectrally) complex objects—a suggestion that has been proposed in the literature [11,12].

Computational order of the al- orithm is a key element in any target-recognition scheme. Since c       irisons are being made across trans-form methods, the analysis will be limited to their respective computational requirements. The FFT is well established at a computational order of $N \log_2 N$; the Gabor basis, which requires an additional $N$-order multiply to window the data before the FFT is performed, also has an $N \log_2 N$ computational order. The Haar basis, which realizes a straightforward butterfly decomposition similar to that of the FFT, can be reduced to a computational order linear in $N$ [39]; thus, the Haar basis outperforms the FFT in both target

recognition and computational complexity. The Gaussian basis used fast convolution, which yields a computational order of $N^2$—the highest of the three. Optimizations similar to the Haar case may be possible; none has been found at this time.

A key point regarding computational order with respect to pruned bases is that the multiresolution decompositions (Haar and Gaussian bases) do not require computation of the spectral coefficients eliminated from the analysis; the FFT, for all intents and purposes, does require a complete projection—the unused coefficients are merely discarded. Although algorithm-pruning methods exist, they are generally difficult to implement, and often result in greater processing time than is required by optimized signal-processing hardware.

A final note on computational requirements: porting the detection and recognition algorithms from PV-WAVE to four i860-based parallel vector processors reduced the single-transform, single-image processing time from 7 hours to about 80 seconds (excluding I/O time). Thus, we can conclude that Fourier- and multiresolution-transform-based target recognition methods are potentially viable schemes for real-time ATR applications.

## 3.7 Conclusions

One is cautioned against drawing too many conclusions from the limited data presented here; although the results are compared against the performance goals for the analysis, true statistical significance can be achieved only with a substantially larger data set. Nevertheless, for the data set analyzed in the course of this research, both the Haar wavelet and the Gaussian multiresolution basis provided target-recognition and false-alarm performance superior to the Fourier bases, with the Gaussian clearly outperforming the Haar in terms of false-alarm rate. The Haar basis remains attractive from a computational standpoint, however.

Regardless of whether the driving consideration is false-alarm rate or inherent computational order (they both, of course, equate to computational order), the multiresolution bases presented in this research have provided target-recognition performance superior to that of the Fourier transform for detection of wideband resonance effects in UWB SAR imagery—including those from targets embedded in foliage.

58

## 3.8 Recommendations for Continued Study

This research provides a point of departure for analysis of wideband resonances through application of linear transform methods; it is not intended to be a comprehensive treatment of the subject. Many related topic areas can benefit from further investigation, some of which are listed below:

- Section 3.4.2.5 suggests that there exists some optimal method of basis pruning; identification of such a method could substantially increase the performance of the bases employed in the analysis.

- Other multiresolution bases should be investigated. Although those employed in this work provided relatively good performance, there is, of course, no guarantee that other bases will not perform better.

- A simple correlation coefficient was calculated in the evaluation of the recognition confidence; other algorithms (such as mean-squared distance) may provide better performance and/or a lower computational load.

- Better target modeling is always desirable, and will certainly be required if the methods presented here are applied to recognition of more complex targets.

- Polar-formatted imagery should improve the performance of all recognition methods and bases investigated. The imagery analyzed in this research was projected onto a Cartesian grid—this results in a geometry-induced defocusing of the target ringdowns, since the "natural" projection grid for SAR data is polar.

(To see the effect of the Cartesian projection, consider that the target ringdown will occur in pixels directly "behind" the target as viewed from each aperture position. Thus, as the aperture is traversed, these ringdowns defocus behind the target. This effect is exacerbated in the near field, which is the mode in which the ARL UWB SAR is operating.)

A potentially viable method for recognition of targets in UWB SAR imagery has been presented; continued investigation into these and other areas will certainly continue to improve the performance of the target-recognition methods presented in this report.

# References

1. L. W. Pearson, M. L. Van Blaricum, and R. Mittra, "A New Method for Radar Target Recognition Based on the Singularity Expansion for the Target," *1975 IEEE International Radar Conference Record* (April 1975), pp 452–457.

2. M. Morgan, "Singularity Expansion Representations of Fields and Currents in Transient Scattering," *IEEE Trans. Antennas Propag.* AP-32, No. 5 (May 1984), pp 466–467.

3. M. A. Morgan and P. D. Larison, "Natural Resonance Extraction from Ultra-Wideband Scattering Signatures," *Ultra-Wideband Radar: Proceedings of the First Los Alamos Symposium*, Bruce Noel (editor), CRC Press, Boca Raton, FL (1991), pp 203–215.

4. J. J. Kovaly, "High Resolution Radar Fundamentals (Synthetic Aperture and Pulse Compression)," *Radar Technology*, E. Brookner (editor), Artech House, Dedham, MA (1978), p 241.

5. R. O. Harger, *Synthetic-Aperture Radar Systems: Theory and Design*, Academic Press, Inc., New York, NY (1970), p 43.

6. W. R. Lawson and J. A. Radches, "A Static Performance Model for Thermal Viewing Systems" (the "Johnson Criteria"), U.S. Army Night Vision Laboratories Report (April 1975), pp 1–60.

7. J. W. McCorkle, "Focusing of Synthetic Aperture Ultra-Wideband Data," *IEEE International Conference on Systems Engineering* (August 1991), p 2.

8. R. K. Young, *Wavelet Theory and its Applications*, Kluwer Academic Publishers, Norwell, MA (1993), pp 82–85.

9. S. Riegger and W. Wiesbeck, "Wideband Polarimetric Signatures as a Basis for Target Classification," *Radar Cross-Sections of Complex Objects*, W. R. Stone (editor), IEEE Press, New York, NY (1990), pp 17–25.

10. S. Cloude, P. Smith, and A. Milne, "Analysis of Time-Domain Ultra-Wideband Radar Signals," *1992 Proc. SPIE* 1631 (1992), pp 111–122.

11. M. L. Van Blaricum and T. L. Larry, "Systems Considerations of Resonance-Based Target Identification," *Ultra-Wideband Radar: Proceedings of the First Los Alamos Symposium*, Bruce Noel (editor), CRC Press, Boca Raton, FL (1991), pp 393–402.

12. J. R. Auton, "Resonance-Based Target Identification Systems," *Ultra-Wideband Radar: Proceedings of the First Los Alamos Symposium*, Bruce Noel (editor), CRC Press, Boca Raton, FL (1991), pp 385–392.

13. H. F. Harmuth, *Nonsinusoidal Waves for Radar and Radio Communication*, Academic Press, New York, NY (1981), pp 114–115.

14. S. Silver, *Microwave Antenna Theory and Design*, McGraw-Hill Book Company, New York, NY (1949), pp 65–99.

15. M. L. Van Blaricum, "A View of the Early-Time Component in Impulsive Scattering," *Ultra-Wideband Radar: Proceedings of the First Los Alamos Symposium*, Bruce Noel (editor), CRC Press, Boca Raton, FL (1991), pp 191–202.

16. R. K. Mains and D. L. Moffatt, "Complex Natural Resonances of an Object in Detection and Discrimination," TR-3424-1, Ohio State University, Electroscience Laboratory, Columbus, OH (June 1974), pp 1–47.

17. T. L. Larry, J. R. Auton, and M. L. Van Blaricum, "Research Efforts in Support of Resonance Extraction Studies, Volume 1: Improvement and Validation of TWFD: A Thin-Wire Frequency-Domain Scattering Code," General Research Corp., Report CR-84-1319 (November 1984), pp 1–23.

18. G. T. Ruck, D. E. Barrick, W. D. Stuart, and C. K. Krichbaum, *Radar Cross-Section Handbook, Volume 2*, Plenum Press, New York, NY (1970), p 574.

19. R. Prony, "Essai experimental et analytique sur les lois de la dilatabilité de fluides élastiques et sur celles de la force d'expansion de la vapeur de l'alkoo, à différentes températures," *J. Ec. Polytech.*, Paris, Vol. 1, No. 2 (1795), pp 24–76.

20. M. L. Van Blaricum and R. Mittra, "Problems and Solutions Associated with Prony's Method for Processing Transient Data," *IEEE Trans. Antennas Propag.* (January 1978), pp 178–182.

21. N. H. Younan, C. M. Shearin, and T. F. Nash, "Natural Frequencies Extraction of a Radar Target from a Measured Response Using the Prony Method," *Record of the 1993 IEEE National Radar Conference* (1993), pp 66–69.

22. J. R. Auton and M. L. Van Blaricum, "Investigation of Procedures for Automatic Resonance Extraction from Noisy Transient Electromagnetic Data," ETI Report CR81-984, ONR Final Report for Contract

N0014-80-C0299; *Vol 1—Investigation of Resonance Extraction Procedures, Vol II—Appendices, Vol III—Translation of Prony's Original Paper and Bibliography of Prony's Method* (August 1981).

23. J. N. Brittingham, E. K. Miller, and J. L. Willows, "The Derivation of Simple Poles in a Transfer Function for Real Frequency Information," Lawrence Livermore Laboratory, UCRL-52050 (April 1974).

24. V. K. Jain, T. K. Sarker, and D. D. Wiener, "Rational Modeling of the Pencil-of-Function Method," *IEEE Trans. Acoust. Speech Signal Process.* ASSP-31 (June 1983), pp 564–573.

25. B. Drachman and E. Rothwell, "A Continuation Method for Identification of the Natural Frequencies of an Object Using a Measured Response," *IEEE Trans. Antennas Propag.* AP-33 (April 1985), pp 445–449.

26. Y. Hua and T. K. Sarker, "Generalized Pencil-of-Function Method for Extracting the Poles of an Electromagnetic System from its Transient Response," *IEEE Trans. Antennas Propag.* 37, No. 2 (February 1989), pp 229–234.

27. R. M. Bracewell, *The Fourier Transform and its Applications*, McGraw-Hill, Inc., New York, NY (1965), chapter 2.

28. A. V. Oppenheim and A. S. Willsky, with I. T. Young, *Signals and Systems*, Prentice-Hall, Englewood Cliffs, NJ (1983), chapter 4.

29. S. A. Tretter, *Introduction to Discrete-Time Signal Processing*, John Wiley & Sons, New York, NY (1976), p 276.

30. A. V. Oppenheim and R. W. Schafer, *Digital Signal Processing*, Prentice-Hall, Inc., Englewood Cliffs, NJ (1975), pp 88–91.

31. J. W. Cooley and J. W. Tukey, "An Algorithm for the Machine Computations of Complex Fourier Series," *Mathematics of Computation*, Vol. 19 (April 1965), pp 297–301.

32. D. Gabor, "Theory of Communication," *J. IEE* 93 (1946), pp 429–457.

33. J. Benedetto, E. Bernstein, D. Colella, M. Dellomo, and G. Jacyna, "A Short Course on Wavelets," course notes from the MITRE presentation to the Army Research Laboratory (October 1992).

34. A. Haar, "Zur Theorie der Orthogonalen Funktionensysteme," *Math. Annal.* 69 (1910), pp 331–371.

35. P. Franklin, "A Set of Continuous Orthogonal Functions," *Math. Annal.* 100 (1928), pp 522–529.

36. O. Rioul and M. Vetterli, "Wavelets and Signal Processing," *IEEE Signal-Processing Magazine* (October 1991), pp 14–38.

37. I. Daubechies, "The Wavelet Transform, Time-Frequency Localization and Signal Analysis," *IEEE Trans. Info. Theory* 36, No. 5 (September 1990), pp 961–1005.

38. F. Hlawatsch and G. F. Boudreaux-Bartels, "Linear and Quadratic Time-Frequency Representations," *IEEE Signal-Processing Magazine* (April 1992), pp 21–67.

39. I. Daubechies, "Orthonormal Bases of Compactly Supported Wavelets," *Commun. Pure Appl. Math.* XLI, John Wiley & Sons, Inc. (1988), pp 910–997.

40. G. Strang, "Wavelets and Dilation Equations: A Brief Introduction," *SIAM Rev.* 31, No. 4 (December 1989), pp 614–627.

41. C. K. Chui (editor), *Wavelets: A Tutorial in Theory and Applications*, Vol. 2 of *Wavelet Analysis and its Applications*, Academic Press, Inc., New York, NY (1992).

42. A. Grossman and J. Morlet, "Decomposition of Hardy Functions into Square-Integrable Wavelets of Constant Shape," *SIAM J. Math. Anal.* 15 (1984), pp 723–736.

43. R.W.P. King, *The Theory of Linear Antennas*, Harvard University Press, Cambridge, MA (1956), pp 50–59, 151–169, 501–511.

44. L. W. Rispin and D. C. Chang, "Wire and Loop Antennas," *Antenna Handbook*, Y. T. Lo and S. W. Lee (editors), Van Nostrand Reinhold Company, New York, NY (1988), chapter 7.

45. D. DeMaw, editor, *The Radio Amateur's Handbook*, 56th edition, The American Radio Relay League, Newington, CT (1979), p 20-3.

# Acknowledgments

# Appendix A. Formation of UWB SAR Images in the Near Field

# Appendix A

## Contents

## Figures

## A-1.     Conventional SAR Image Formation

### A-1.1     *General Range/Doppler Processing*

Pulse compression (for increased range resolution) and synthetic-aperture generation (for increased azimuth resolution) are independent processes; that is, a synthetic-aperture radar (SAR) uses the same pulse-ranging technique as a real-aperture radar, yielding a deramped bandwidth in which range is a function of frequency. Equi-frequency points map into equi-range points (which are concentric circles centered at the radar) through an inverse Fourier transform.

Real-aperture systems are resolution-limited in azimuth by the beamwidth of the radar antenna (other factors being assumed constant). Synthetic-aperture systems overcome this limitation through the Doppler beam-sharpening concept: relative motion of the radar with respect to the target provides a Doppler signature, which can be coherently processed so that the main antenna beam is effectively split into multiple narrower ("sharper") beams. Typically, the radar is placed on an airborne platform, with the physical beam oriented 90° to the velocity vector of the vehicle (some applications, such as missile homing systems, use orientations—"squints"—at angles other than 90°). As the radar traverses the field of view, stationary objects within the field will exhibit strictly decreasing Doppler shifts as they "move" through the field of view from front to rear. The intersection of the conical equi-Doppler surfaces with the image plane yields hyperbolas of equal Doppler ("isodops") in the image plane. Thus, Doppler-shift frequencies induced by the motion of the radar platform map into angular position along isodops; similar to the pulse-ranging case, the image generated by this mapping can easily be formed through an inverse Fourier transform.

Since position in both range and azimuth can be resolved in a straightforward manner through inverse fast Fourier transforms (FFT's), the two-dimensional (2-D) inverse FFT (IFFT) has ofter. been the preferred method of SAR image formation. The 2-D IFFT approach, however, has limitations that can make it undesirable in certain applications. Ultra-wide bandwidths render interpretation of coherency and phase meaningless in many instances, while near-field phenomena require substantial modifications to Fourier-based aperture functions. For example, the Doppler paradigm, while useful for understanding the synthetic-aperture focusing operation in narrowband applications, breaks down in the wide band. Doppler shift—defined as $2v/\lambda$ for a platform moving at velocity $v$—is helpful in describing the beam-sharpening concept when $\lambda$ varies by a

# Appendix A

small percentage, but fails direct interpretation in the wide band, where $\lambda$ can vary by 10 to 1 or more. Thus, to fully comprehend the ultra-wideband (UWB) SAR image-formation process where neither bandwidth nor geometry is restricted, it is useful to view the synthetic aperture as a coherent linear array of $N$ transmitter/receivers.[1] The pitfalls of Fourier-based image formation are straightforwardly presented in the antenna-array conceptualization.

## A-1.2 Effects of Unconstrained Bandwidth and Geometry on SAR Image Formation

Synthetic-aperture image formation can be viewed as a "beam-forming" process, whereby backscattered signals are coherently added to form antenna beams in the direction from which the scattering occurred. Each aperture position, or synthetic-aperture sampling point, is viewed as a discrete physical antenna, in which the contributions from each antenna add coherently with the rest of the array; the "boresight" of the array will be defined as a line extending in range orthogonal to the azimuthal axis of the array. In this representation, incident planar echoes from a distant, boresighted target reach all points along the aperture simultaneously, exciting all points of the aperture in phase (fig. A-1a); at any instant in time, this yields a dc voltage across the array. If the target is moved off the boresight, backscattered returns will excite the elements of the array out of phase, producing a sinusoidal response across the array (fig. A-1b). The oscillation rate along the aperture increases as the target moves farther off the boresight (fig. A-1c), yielding azimuth position

Figure A-1. Fourier beam forming: (a) backscattered wavefronts from a boresighted target; (b), (c) wavefronts fr�� off-boresight targets.
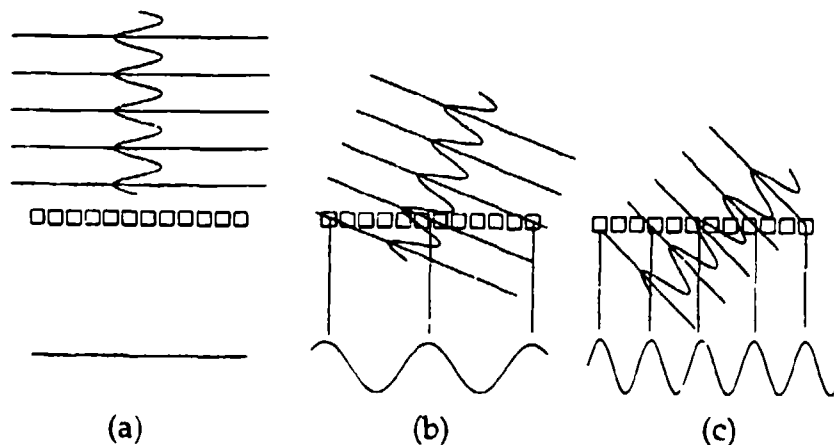


(a)                    (b)                    (c)

---

[1] J. W. McCorkle, "Focusing of Synthetic Aperture Ultra-Wideband Data," IEEE International Conference on Systems Engineering (August 1991), p 2.

as a function of oscillation frequency, in a manner similar to the Doppler case.

### A-1.1.1  Bandwidth-Related Aliasing Effects

The mapping from oscillation frequency to azimuth position is straightforward in the narrow band. If we now remove bandwidth constraints, we find that—for identical azimuth positions—the frequency of oscillation is no longer strictly a one-to-one mapping in azimuth, but is also a function of wavelength (fig. A-2). This introduces ambiguities into the mapping function that—if not accounted for—will yield a poorly focused image, an effect that is exacerbated as the relative bandwidth increases. The solution to this problem requires dividing the system bandwidth into narrower subbands; narrowband approximations can then be employed to form multiple beams at each aperture position, and the wideband image can be constructed through superposition of each of the narrowband images. Superposition of the images requires that the beams formed for each subband have the same beamwidth; since beamwidth is a function of wavelength and aperture size, forming equi-angle beams requires that the effective aperture length be modified for each subband. Since the sampling rate along the aperture must remain constant, the result is substantial oversampling of the aperture—obviously, a very undesirable effect. Additionally, this method is computationally intensive.

### A-1.1.2  Near-Field Effects

If we now move the target into the near field, we find that boresighted target returns no longer excite the array elements in phase, because of the curvature of the wavefront (fig. A-3a). We can compensate for this phenomenon by application of polar formatting, which effectively "curves" the aperture to match that of the wavefront, thereby simulating a planar return and causing the array ele-

Figure A-2. Azimuth aliasing in wide band: (a) correct azimuth position at frequency 1 ($f_1$); (b) incorrect position calculated for $f_2 \neq f_1$.
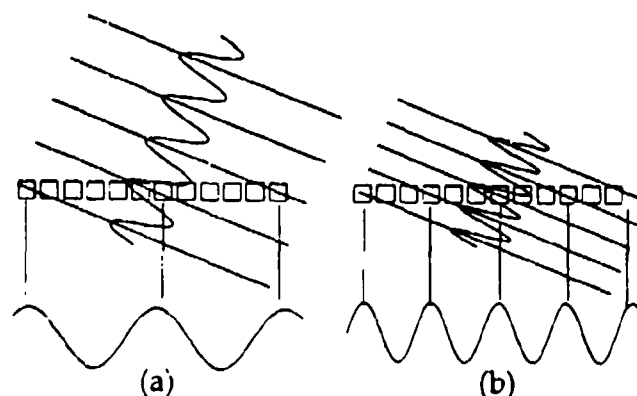
# Appendix A

ments to once again be excited in phase (fig. A-3b). We can accomplish this by time-shifting the target returns at each aperture point so that the aperture behaves as if it were curved, with the target positioned at the center of curvature;[1] the result is a dc value across the aperture at any instant in time. Unfortunately, this solution focuses the image only at the center of curvature, and begins to defocus as range and azimuth angle diverge from that point. To see this, consider the near-field corrected aperture of figure A-3b; now, an off-boresight target will excite a sinusoidal response across the array (fig. A-3c). One solution to this problem is to calculate the polar-format aperture corrections at every point in the image; for most applications, this approach is computationally prohibitive. Another solution requires that a specified amount of defocusing be accepted in the image, and aperture corrections be made for "patches" in the image. In this scheme, each patch is perfectly focused at the center, and begins to defocus in range and azimuth toward the edges of the patch. The resultant image is thus a mosaic of imperfectly focused patches, but this method is much less computationally intensive than the method of computing aperture corrections at each point in the image.

The combination of wideband aliasing and polar formatting effects in UWB near-field SAR restricts Fourier-based image formation to very small patches in the image, if reasonably high image quality is desired.[1] Similar problems, such as range walk and wavefront curvature, also serve to limit the efficacy of Fourier techniques in near-field applications. Overall, Fourier techniques require substantial processing to form UWB images in the near field; thus, some form of image formation is desired that uses the entire signal bandwidth and aperture simultaneously, while still preserving target resonance effects. One method of forming synthetic-aperture images in unconstrained bandwidth/geometry scenarios is the "backprojection"

Figure A-3. Polar formatting in near field: (a) uncorrected aperture for bore-sighted target; (b) corrected aperture for boresighted target; and (c) uncorrected aperture for off-boresight target.
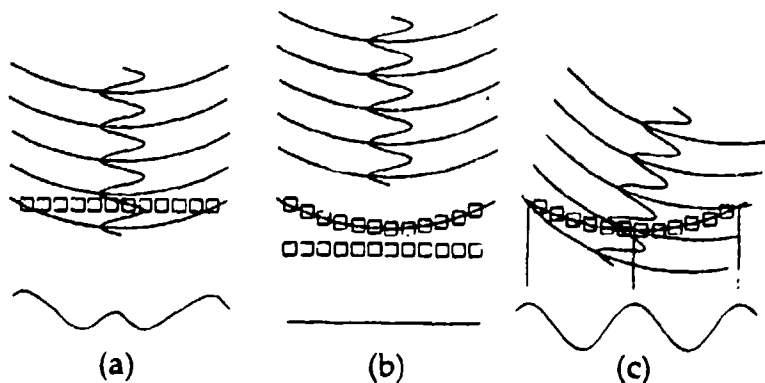


(a)    (b)    (c)

[1] J. W. McCorkle, "Focusing of Synthetic Ape  ..e Ultra-Wideband Data," IEEE International Conference on Systems Engineering (August 1991), p 2.

method (also known as the "summation" method), a technique commonly employed in computerized tomography (CT) for medical imaging. I present an adaptation of the backprojection image-formation method to the SAR mode.

## A-2. Backprojection of UWB SAR Imagery

The treatment of the SAR-mode backprojection algorithm presented in this section is adapted from McCorkle and Nguyen.[2] Analogs to CT are from Herman.[3] The treatment here is brief; more detailed descriptions can be found in the works cited.

The backprojection algorithm employed in computerized tomography involves addition of all the ray values (the received signals) of all the rays (the transmitted signals) passing through a point (where the point contributes an attenuation factor to the transmitted signal). One can generate a 2-D "attenuation map" by repeating this process for every point in the field of view. This is an inherently near-field process, as the transmitter and receiver rotate in a coordinated manner around the field of points generating the map.

The SAR mode is slightly different. In SAR, a "reflectivity map" is generated from the radar echoes of scatterers in the image; thus, the key values in the process are contributions instead of attenuations. Replacing the bistatic CT case with a monostatic SAR, we find that the fundamental concepts remain largely unchanged. If we view a received radar echo as a ray from the target to the receiver, the scatterer-modified CT image-focusing criteria apply equally to SAR:

- The ray can contribute only to those pixels on the image grid that it intersects, and no others.

- The contribution of the ray to any pixel that it intersects must be proportional to the ray's signal strength, $y_j$ (where $y_j$ denotes the signal strength, $y$, of the $j^{th}$ ray).

- The contribution of the ray to any pixel that it intersects should be proportional to the length of the intersection of the ray with the pixel (i.e., the ray's contribution to the pixel will be proportionally greater if the ray bisects the pixel than if it grazes the pixel). We define this intersection length as $r_{i,k,j}$, where the indices $(i,k)$ denote the image-grid position of the pixel intersected by the ray $j$.

---

[2] J. W. McCorkle and L. Nguyen, Ultra-wide Bandwidth Synthetic Aperture Radar Focusing of Dispersive Targets, Army Research Laboratory, ARL-TR-305 (April 1994).

[3] G. T. Herman, Image Reconstruction from Projections, Academic Press, Inc., Orlando, FL (1980), chapter 7.

# Appendix A

These criteria are satisfied by

$$x_{i,k}^* \approx \sum_j r_{i,k,j} y_j \, ,$$ 

<div align="right">(A-1)</div>

where $x_{i,k}^*$ is the estimate of the absorption (or reflectivity) contribution from the $(i,k)^{th}$ pixel on the image grid. This is a general result for any data-collection scheme;[3] we can now apply this result to the SAR-specific mode.

The fundamental backprojection geometry is shown in figure A-4; note that bearing lines are graduated in $k$, radial distance (polar range) is graduated in $i$, and aperture position is graduated in $j$. Positions on the image grid (as well as positions along the aperture) are referenced to the center of the aperture. The radial distance from the $j^{th}$ position in the aperture to the $(i,k)^{th}$ position in the image area is denoted $d_{i,k,j}$.

Consider an isotropic scatterer in empty space, with the scatterer at position $(i,k)$ on the image grid; assume that an ideal impulse $\delta(t)$ is broadcast. For the contributions of the backscattered energy to be maximized, the echo energy from the scatterer must be coherently summed across the aperture. Coherency, however, is defined by phase angle; hence, the usual (narrowband) interpretation of coherent addition cannot be used, because the ARL UWB SAR is operating in the wide band. Equation (A-1) provides a frequency-indepen-

**Figure A-4.
Backprojection
image-area geometry.**
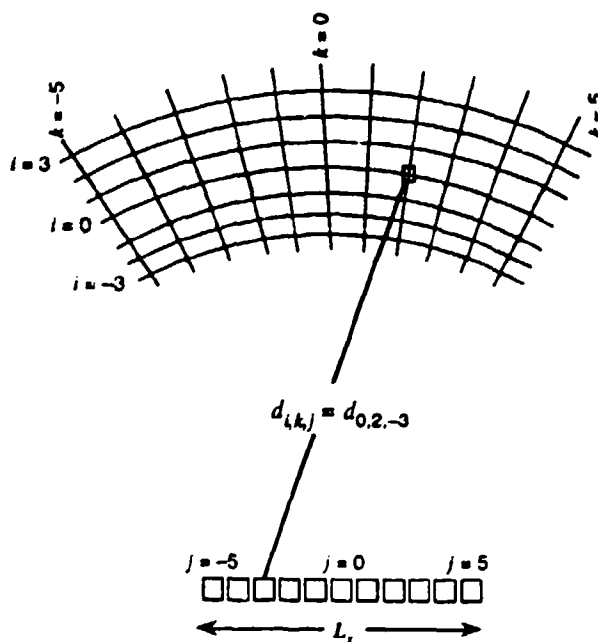


$$d_{i,k,j} = d_{0,2,-3}$$

3G. T. Herman, Image Reconstruction from Projections, Academic Press, Inc., Orlando, FL (1980), chapter 7.

72

dent means of summing the echoes while preserving coherency across the band. For the wideband SAR case, the general reflectivity (or absorption, in CT) term $x_{ik}^*$ in (A-1) is the wideband RCS of the target, which in this case is the response of the scatterer to the incident impulse $\delta(t)$. The signal-strength and intersection-length terms in the summation of (A-1) can be replaced with $s_j(t)$, the received signal amplitude (in volts) as a function of time (in seconds, from the leading edge of the transmitted pulse) at the $j^{th}$ position in the aperture (conceptually equivalent to the magnitude of the $j^{th}$ ray). Thus, we arrive at the definition of the impulse response of an isotropic scatterer at position $(i,k)$ on the image grid:

$$x_{ik}^*(t) = \sum_j s_j(T_{ik,j} + t), \quad t \geq 0 . \tag{A-2}$$

This development assumes that the scatterer is isotropic within the plane of the radar (a vertical dipole, for example). In general, of course, the impulse response of the target will be a function of aspect angle (hence, aperture position). In theory, we can accommodate this effect at each point in the aperture by defining a set of matched filters $F$, where each filter $F_j$, defined for a specific aperture position $j$, is matched to the target's impulse response at that aspect angle:

$$x_{ik}^*(t) = \sum_j [F_j \otimes s_j](T_{ik,j} + t), \quad t \geq 0 . \tag{A-3}$$

Obviously, this is not a plausible scenario in realistic applications, and thus equation (A-2) suffices in the formation of images by backprojection.

Note that (A-2) can lead to a significant computational requirement if $x_{ik}^*(t)$ is calculated for every point in the aperture; methods have been devised that substantially reduce this processing load.[2]

The method of image formation outlined in this section is very general,[3] and specifically provides the capability to focus near-field synthetic-aperture images of dispersive targets with a lower computational order than is required by Fourier-based image formation techniques.[2] For these reasons, backprojection is the method of image formation employed in the ARL UWB SAR instrumentation system.

---

[2] J. W. McCorkle and L. Nguyen, Ultra Wide Bandwidth Synthetic Aperture Radar Focusing of Dispersive Targets, Army Research Laboratory, ARL-TR-305 (April 1994).

[3] G. T. Herman, Image Reconstruction from Projections, Academic Press, Inc., Orlando, FL (1980), chapter 7.

# Appendix B. Detailed Spectral Data

# Appendix B

## Contents

## Tables

The following tables identify the spectral coefficients employed for each basis in the analysis. Complete bases for the 114.3-cm dipole are presented in section B-1; pruned bases are in B-2. Complete bases for the 166.4-cm dipole are presented in section B-3; no pruning was performed on these bases.

## B-1. Complete Bases—114.3-cm Dipole

### B-1.1 Fourier Basis

Table B-1. Fourier-basis spectral coefficients: 114.3-cm dipole, complete basis.

| Coefficient number | Spectral value | |
|---|---|---|
| | Real | Imaginary |
| 0 | –318.348 | 0.00000 |
| 1 | –214.043 | 298.915 |
| 2 | –516.904 | –2020.44 |
| 3 | 161.738 | 174.988 |
| 4 | 75.8170 | –44.9084 |
| 5 | –90.4951 | –14.1315 |
| 6 | 44.1456 | 469.620 |
| 7 | 213.181 | –0.282646 |
| 8 | 119.745 | –27.0265 |
| 9 | 115.782 | 17.5103 |
| 10 | 136.794 | –91.1553 |
| 11 | 31.5088 | –120.760 |
| 12 | –3.54461 | –79.9276 |
| 13 | –13.4296 | –66.9845 |
| 14 | –87.6190 | –26.6449 |
| 15 | –5.50098 | 16.0659 |
| 16 | 7.12519 | 5.17419 |
| 17 | 11.4464 | 0.998665 |
| 18 | 13.4641 | –1.63380 |
| 19 | 14.1127 | –3.54582 |
| 20 | 13.7892 | –4.74643 |
| 21 | 13.0774 | –5.17873 |
| 22 | 12.3533 | –5.02351 |
| 23 | 11.8466 | –4.56626 |
| 24 | 11.5068 | –4.01206 |
| 25 | 11.2853 | –3.44555 |
| 26 | 11.1333 | –2.86084 |
| 27 | 11.0731 | –2.29099 |
| 28 | 11.0778 | –1.76971 |
| 29 | 11.0964 | –1.32471 |
| 30 | 11.0774 | –0.909546 |
| 31 | 11.0312 | –0.474152 |
| 32 | 11.0069 | 0.00000 |

# Appendix B

## B-1.2  Gabor-Wavelet Basis

Table B-2. Gabor-basis spectral coefficients: 114.3-cm dipole, complete basis.

| Coefficient number | Spectral value | |
|---|---|---|
| | Real | Imaginary |
| 0 | –50.9963 | 0.00000 |
| 1 | 62.0448 | 219.153 |
| 2 | –72.8635 | –324.768 |
| 3 | 46.0480 | 229.264 |
| 4 | –1.98621 | –71.8854 |
| 5 | –15.2368 | –27.7820 |
| 6 | –0.729738 | 64.4972 |
| 7 | 16.3227 | –42.5209 |
| 8 | –10.3434 | 9.20498 |
| 9 | –0.798927 | 3.99802 |
| 10 | 7.99257 | –2.50583 |
| 11 | –5.46995 | –3.25999 |
| 12 | –1.27268 | 3.54381 |
| 13 | 7.04654 | –2.32910 |
| 14 | –10.6560 | –0.609302 |
| 15 | 6.78050 | 3.00796 |
| 16 | –1.69493 | –1.65300 |
| 17 | 0.181264 | 0.340625 |
| 18 | 0.0225425 | –0.0237844 |
| 19 | 0.0275464 | –0.00541973 |
| 20 | 0.0122311 | –0.0131955 |
| 21 | 0.00910687 | –0.0100573 |
| 22 | 0.00210452 | –0.00484216 |
| 23 | 0.00670195 | –0.00210416 |
| 24 | 0.00562000 | –0.00108862 |
| 25 | 0.00737572 | –0.00284195 |
| 26 | 0.00469398 | –0.00115204 |
| 27 | 0.00564241 | –0.000623703 |
| 28 | 0.00635052 | 0.00126266 |
| 29 | 0.00796127 | –0.000312805 |
| 30 | 0.0074577 | –0.000991821 |
| 31 | 0.00603294 | –0.00151062 |
| 32 | 0.00525665 | 0.00000 |

78

## B-1.3 Haar Basis

**Table B-3. Haar-wavelet spectral coefficients: 114.3-cm dipole, complete basis.**

| Coefficient number | Spectral value | Coefficient number | Spectral value |
|---|---|---|---|
| 0 | −318.348 | 32 | −40.3743 |
| 1 | −412.075 | 33 | 424.285 |
| 2 | 1969.31 | 34 | −753.142 |
| 3 | 2730.24 | 35 | −871.667 |
| 4 | −650.079 | 36 | 565.207 |
| 5 | 1145.55 | 37 | 175.250 |
| 6 | −1021.26 | 38 | 376.486 |
| 7 | 971.844 | 39 | −39.5327 |
| 8 | −910.263 | 40 | 4.33569 |
| 9 | 1115.19 | 41 | 226.673 |
| 10 | 1962.04 | 42 | 838.519 |
| 11 | −1396.46 | 43 | 591.859 |
| 12 | −1917.93 | 44 | −203.073 |
| 3 | 178.41 | 45 | −279.472 |
| 14 | 1687.99 | 46 | −487.526 |
| 15 | −926.336 | 47 | −196.120 |
| 16 | 361.831 | 48 | −306.369 |
| 17 | −2164.12 | 49 | −415.742 |
| 18 | 763.495 | 50 | −599.436 |
| 19 | 400.718 | 51 | −396.019 |
| 20 | 238.206 | 52 | 82.9497 |
| 21 | 1649.73 | 53 | 242.144 |
| 22 | −481.098 | 54 | 404.953 |
| 23 | −704.551 | 55 | 261.642 |
| 24 | −753.249 | 56 | 358.186 |
| 25 | −1099.64 | 57 | 415.441 |
| 26 | 323.354 | 58 | 468.311 |
| 27 | 674.244 | 59 | 306.450 |
| 28 | 797.703 | 60 | −12.2661 |
| 29 | 830.236 | 61 | −178.096 |
| 30 | −189.395 | 62 | −323.860 |
| 31 | −616.250 | 63 | −287.776 |

# Appendix B

## B-1.4    *Gaussian Basis*

Table B-4. Gaussian-basis spectral coefficients: 114.3-cm dipole, complete basis.

| Coefficient number | Spectral value | Coefficient number | Spectral value |
|---|---|---|---|
| 0 | -4478.20 | 16 | 286.460 |
| 1 | 1420.85 | 17 | 558.907 |
| 2 | 3969.81 | 18 | 112.563 |
| 3 | 5065.19 | 19 | 103.262 |
| 4 | -7784.11 | 20 | -724.114 |
| 5 | 7366.77 | 21 | -1050.48 |
| 6 | -6493.34 | 22 | -458.221 |
| 7 | -785.665 | 23 | -33.8032 |
| 8 | 1249.36 | 24 | 760.483 |
| 9 | -430.782 | 25 | 1015.33 |
| 10 | -2825.20 | 26 | 516.326 |
| 11 | 1091.52 | 27 | 10.3358 |
| 12 | 2857.55 | 28 | -683.137 |
| 13 | -1139.60 | 29 | -918.706 |
| 14 | -2713.72 | 30 | -530.018 |
| 15 | -17.7338 | | |

## B-2. Pruned Bases—114.3-cm Dipole

### B-2.1 Fourier Basis

**Table B-5. Fourier-basis spectral coefficients: 114.3-cm dipole, pruned basis.**

| Coefficient number | Spectral value | |
|---|---|---|
| | Real | Imaginary |
| 0 | –318.348 | 0.00000 |
| 1 | –214.043 | 298.915 |
| 2 | –516.904 | –2020.44 |
| 3 | 161.738 | 174.988 |
| 4 | 75.8170 | –44.9084 |
| 5 | –90.4951 | –14.1315 |
| 6 | 44.1456 | 469.620 |
| 7 | 213.181 | –0.282646 |
| 8 | 119.745 | –27.0265 |
| 9 | 115.782 | –17.5103 |
| 10 | 136.794 | –91.1553 |
| 11 | 31.5088 | –120.760 |
| 12 | –3.54461 | –79.9276 |
| 13 | –13.4296 | –66.9845 |
| 14 | –87.6190 | –26.6449 |
| 15 | –5.50098 | 16.0659 |
| 16 | 7.12519 | 5.17419 |
| 17 | 11.4464 | 0.998665 |
| 18 | 13.4641 | –1.63380 |
| 19 | 14.1127 | –3.54582 |
| 20 | 13.7892 | –4.74643 |
| 21 | 13.0774 | –5.17873 |
| 22 | 12.3533 | –5.02351 |
| 23 | 11.8466 | –4.56626 |
| 24 | 11.5068 | –4.01206 |
| 25 | 11.2853 | –3.44555 |
| 26 | 11.1333 | –2.86084 |
| 27 | 11.0731 | –2.29099 |
| 28 | 11.0778 | –1.76971 |
| 29 | 11.0964 | –1.32471 |
| 30 | 11.0774 | –0.909546 |
| 31 | 11.0312 | –0.474152 |

# Appendix B

## B-2.2 Gabor Basis

Table B-6. Gabor-basis spectral coefficients: 114.3-cm dipole, pruned basis.

| Coefficient number | Spectral value | |
|---|---|---|
| | Real | Imaginary |
| 0 | −50.9963 | 0.00000 |
| 1 | 62.0448 | 219.153 |
| 2 | −72.8635 | −324.768 |
| 3 | 46.0480 | 229.264 |
| 4 | −1.98621 | −71.8854 |
| 5 | −15.2368 | −27.7820 |
| 6 | −0.729738 | 64.4972 |
| 7 | 16.3227 | −42.5209 |
| 8 | −10.3434 | 9.20498 |
| 9 | −0.798927 | 3.99802 |
| 10 | 7.99257 | −2.50583 |
| 11 | −5.46995 | −3.25999 |
| 12 | −1.27268 | 3.54381 |
| 13 | 7.04654 | −2.32910 |
| 14 | −10.6560 | −0.609302 |
| 15 | 6.78050 | 3.00796 |
| 16 | −1.69498 | −1.65300 |
| 17 | 0.181264 | 0.340625 |
| 18 | 0.0225425 | −0.0237844 |
| 19 | 0.0275464 | −0.00541973 |
| 20 | 0.0122311 | −0.0131955 |
| 21 | 0.00910687 | −0.0100573 |
| 22 | 0.00210452 | −0.00484216 |
| 23 | 0.00670195 | −0.00210416 |
| 24 | 0.00562000 | −0.00108862 |
| 25 | 0.00737572 | −0.00284195 |
| 26 | 0.00469398 | −0.00115204 |
| 27 | 0.00564241 | −0.000623703 |
| 28 | 0.00635052 | 0.00126266 |
| 29 | 0.00796127 | −0.000312805 |
| 30 | 0.00745773 | −0.000991821 |
| 31 | 0.00603294 | −0.00151062 |

## B-2.3 Haar Basis

Table B-7. Haar-wavelet spectral coefficients: 114.3-cm dipole, pruned basis.

| Coefficient number | Spectral value | Coefficient number | Spectral value |
|---|---|---|---|
| 0 | -318.348 | 18 | 797.703 |
| 1 | -412.075 | 19 | -40.3743 |
| 2 | 1969. 1 | 20 | 424.285 |
| 3 | 2730.24 | 21 | -753.142 |
| 4 | -650.079 | 22 | -871.667 |
| 5 | 1145.55 | 23 | 565.207 |
| 6 | -1021.26 | 24 | 838.519 |
| 7 | -910.263 | 25 | -487.526 |
| 8 | 1962.04 | 26 | -306.369 |
| 9 | -1396.46 | 27 | -599.436 |
| 10 | -1917.93 | 28 | 358.186 |
| 11 | 1178.41 | 29 | 415.441 |
| 12 | 1687.99 | 30 | 468.311 |
| 13 | -926.336 | 31 | 306.450 |
| 14 | 361.831 | 32 | -12.2661 |
| 15 | -2164.12 | 33 | -178.096 |
| 16 | 1649.73 | 34 | -323.860 |
| 17 | -1099.64 | 35 | -287.776 |

## B-2.4 Gaussian Basis

Table B-8. Gaussian-basis spectral coefficients: 114.3-cm dipole, pruned basis.

| Coefficient number | Spectral value | Coefficient number | Spectral value |
|---|---|---|---|
| 0 | -4478.20 | 15 | 558.907 |
| 1 | 1420.85 | 16 | 112.563 |
| 2 | 3969.81 | 17 | 103.262 |
| 3 | 5065.19 | 18 | -724.114 |
| 4 | -7784.11 | 19 | -1050.48 |
| 5 | 7366.77 | 20 | -458.221 |
| 6 | -6493.34 | 21 | -33.8032 |
| 7 | 1249.36 | 22 | 760.483 |
| 8 | -2825.20 | 23 | 1015.33 |
| 9 | 1091.52 | 24 | 516.326 |
| 10 | 2857.55 | 25 | 10.3358 |
| 11 | -1139.60 | 26 | -683.137 |
| 12 | -2713.72 | 27 | -918.706 |
| 13 | -17.7338 | 28 | -530.018 |
| 14 | 286.460 | — | — |

# Appendix B

## B-3. Complete Bases—166.4-cm Dipole

### B-3.1 Fourier Basis

Table B-9. Fourier-basis spectral coefficients: 166.4-cm dipole, complete basis.

| Coefficient number | Spectral value | |
|---|---|---|
| | Real | Imaginary |
| 0 | 155.794 | 0.00000 |
| 1 | 842.386 | 121.711 |
| 2 | -271.411 | -500.053 |
| 3 | 280.990 | -165.962 |
| 4 | -387.522 | 92.6497 |
| 5 | -51.7679 | -123.051 |
| 6 | 112.217 | -32.6778 |
| 7 | -135.732 | 99.3113 |
| 8 | -48.7457 | -36.4133 |
| 9 | 9.97179 | 21.9274 |
| 10 | -73.0809 | 0.753423 |
| 11 | -31.2626 | -21.6165 |
| 12 | -33.3348 | 3.34908 |
| 13 | -37.5577 | -17.3137 |
| 14 | -25.5063 | -17.3839 |
| 15 | -24.9856 | -15.7142 |
| 16 | -20.5201 | -17.2109 |
| 17 | -16.5656 | -15.5480 |
| 18 | -14.3222 | -13.2945 |
| 19 | -13.0861 | -11.3297 |
| 20 | -12.3304 | -9.72575 |
| 21 | -11.8306 | -8.40200 |
| 22 | -11.4382 | -7.27959 |
| 23 | -11.1068 | -6.23325 |
| 24 | -10.9137 | -5.23159 |
| 25 | -10.8590 | -4.35902 |
| 26 | -10.8363 | -3.63212 |
| 27 | -10.7953 | -2.98314 |
| 28 | -10.7467 | -2.37737 |
| 29 | -10.6837 | -1.79269 |
| 30 | -10.6216 | -1.19049 |
| 31 | -10.5992 | -0.581936 |
| 32 | -10.6011 | -0.00000 |

## B-3.2  Gabor Basis

Table B-10. Gabor-
basis spectral
coefficients: 166.4-cm
dipole, complete
basis.

| Coefficient number | Spectral value | |
| --- | --- | --- |
| | Real | Imaginary |
| 0 | −153.289 | 0.00000 |
| 1 | 162.400 | −53.5448 |
| 2 | −156.440 | 59.7848 |
| 3 | 127.778 | −13.5210 |
| 4 | −84.7642 | −26.6836 |
| 5 | 23.8562 | 26.1450 |
| 6 | 20.4341 | −1.47396 |
| 7 | −24.5748 | −17.6055 |
| 8 | 6.16998 | 18.0633 |
| 9 | 8.11839 | −9.37920 |
| 10 | −10.2153 | 1.11616 |
| 11 | 5.34816 | 3.32283 |
| 12 | −0.966001 | −3.81853 |
| 13 | −1.03745 | 2.17067 |
| 14 | 1.03316 | −0.438081 |
| 15 | −0.545132 | −0.176550 |
| 16 | 0.102180 | 0.240295 |
| 17 | 0.0275498 | −0.0353552 |
| 18 | −0.00494087 | 0.00388557 |
| 19 | −0.00555599 | 0.00526774 |
| 20 | −0.00391239 | 0.00515366 |
| 21 | −0.00630164 | 0.00308573 |
| 22 | −0.00741911 | 0.00583124 |
| 23 | −0.00314236 | 0.00573063 |
| 24 | −0.00270629 | 0.000896454 |
| 25 | −0.00668144 | −8.86917e-05 |
| 26 | −0.00715160 | 0.00215673 |
| 27 | −0.00570107 | 0.00155163 |
| 28 | −0.00666428 | 0.000817299 |
| 29 | −0.00656128 | 0.00213718 |
| 30 | −0.00468445 | 0.00123787 |
| 31 | −0.00553894 | −0.000944138 |
| 32 | −0.0070£719 | 0.00000 |

# Appendix B

## B-3.3  Haar Basis

Table B-11. Haar-wavelet spectral coefficients: 166.4-cm dipole, complete basis.

| Coefficient number | Spectral value | Coefficient number | Spectral value |
|---|---|---|---|
| 0 | 155.794 | 32 | -221.686 |
| 1 | 114.876 | 33 | -38.7012 |
| 2 | 269.799 | 34 | 142.952 |
| 3 | -1651.21 | 35 | -53.9926 |
| 4 | 109.578 | 36 | -14.0844 |
| 5 | 1455.16 | 37 | 39.8749 |
| 6 | -794.996 | 38 | 108.954 |
| 7 | -749.856 | 39 | 71.9592 |
| 8 | 36.6732 | 40 | -112.063 |
| 9 | 266.106 | 41 | -343.393 |
| 10 | -980.033 | 42 | -311.842 |
| 11 | 955.627 | 43 | 305.661 |
| 12 | -579.728 | 44 | 620.157 |
| 13 | 166.376 | 45 | 269.477 |
| 14 | -762.751 | 46 | 134.966 |
| 15 | 298.787 | 47 | 139.914 |
| 16 | ·465.034 | 48 | 30.7699 |
| 17 | 43.7898 | 49 | -101.723 |
| 18 | 15.6279 | 50 | -209.574 |
| 19 | 198.123 | 51 | -226.604 |
| 20 | -460.418 | 52 | -104.065 |
| 21 | -53.7968 | 53 | 67.2802 |
| 22 | 912.990 | 54 | 85.7187 |
| 23 | 287.332 | 55 | -102.882 |
| 24 | -71.8227 | 56 | -232.326 |
| 25 | -452.588 | 57 | -195.090 |
| 26 | -30.9309 | 58 | -178.009 |
| 27 | -3.02547 | 59 | —176.367 |
| 28 | -436.778 | 60 | -105.670 |
| 29 | -360.332 | 61 | 16.0564 |
| 30 | -93.4034 | 62 | 143.239 |
| 31 | 366.571 | 63 | 211.862 |

## B-3.4   *Gaussian Basis*

Table B-12. Gaussian-basis spectral coefficients: 166.4-cm dipole, complete basis.

| Coefficient number | Spectral value | Coefficient number | Spectral value |
|---|---|---|---|
| 0 | −9920.62 | 16 | 102.444 |
| 1 | 1485.52 | 17 | 144.040 |
| 2 | −880.968 | 18 | 29.1049 |
| 3 | 968.286 | 19 | 71.6920 |
| 4 | 2001.88 | 20 | 546.099 |
| 5 | −1617.14 | 21 | −134.097 |
| 6 | 3484.67 | 22 | −478.978 |
| 7 | 681.320 | 23 | −607.070 |
| 8 | 383.840 | 24 | −364.902 |
| 9 | 1169.61 | 25 | −112.063 |
| 10 | −1272.48 | 26 | −214.072 |
| 11 | −1845.40 | 27 | 39.4208 |
| 12 | −555.947 | 28 | 339.390 |
| 13 | 690.788 | 29 | 557.405 |
| 14 | 1903.94 | 30 | 433.231 |
| 15 | 154.830 | | |

# Appendix C. Detailed Results of Analyses

# Appendix C

## Contents

## Tables

This appendix tabulates the detailed results of the individual analyses. The first table in each section herein was also presented in section 3.5 in the main body of the report; these results are repeated here for ease of comparison with the rest of the results detailed in this section. The second tables in the first three sections (C-2.1 through C-2.3) identify the number of recognitions for each target and transform method. The last column in the second table in these sections lists the maximum false-alarm correlation for each transform method. The results are tabulated in a combined manner in the remaining sections.

## C-1.    Image 1: Complete Bases

Image 1 is for Run 1, west-west polarized; there are four 114.3-cm targets in the image. Table C-1 gives correlation values.

Table C-1. Image 1 recognition performance: Correlation values, complete bases.

| Transform method | Target correlation coefficients by dipole orientation | | | | Thresh-old | No. false alarms |
|---|---|---|---|---|---|---|
| | Vertical | East | West | Horizontal | | |
| FFT | 0.592 | 0.514 | 0.719 | 0.811 | 0.50 | 8,855 |
| Gabor | 0.629 | 0.610 | 0.825 | 0.887 | 0.60 | 1,636 |
| Haar | 0.348 | 0.304 | 0.357 | 0.371 | 0.30 | 63,527 |
| Gaussian | 0.872 | 0.801 | 0.927 | 0.912 | 0.80 | 1,056 |

*(Note: In this example, the thresholds were set so that a single recognition was guaranteed for each transform method.)*

## C-2.    Image 1: Pruned Bases

Table C-2 gives values correlation for the pruned bases of image 1; table C-3 gives the number of recognitions.

Table C-2. Image 1 recognition performance: Correlation values, pruned bases.

| Transform method | Target correlation coefficients by dipole orientation | | | | Thresh-old | No. false alarms |
|---|---|---|---|---|---|---|
| | Vertical | East | West | Horizontal | | |
| FFT | 0.658 | 0.606 | 0.808 | 0.922 | 0.60 | 8,709 |
| Gabor | 0.699 | 0.668 | 0.947 | 0.985 | 0.66 | 18,131 |
| Haar | 0.759 | 0.627 | 0.853 | 0.921 | 0.60 | 4,845 |
| Gaussian | 0.904 | 0.840 | 0.915 | 0.977 | 0.80 | 1,146 |

Table C-3. Image 1 recognition performance: Number of recognitions.

| Transform method | Target correlation coefficients by dipole orientation | | | | Max false-alarm correlation |
|---|---|---|---|---|---|
| | Vertical | East | West | Horizontal | |
| FFT | 12 | 2 | 64 | 110 | 0.89 |
| Gabor | 13 | 12 | 54 | 105 | 0.98 |
| Haar | 16 | 16 | 36 | 76 | 0.85 |
| Gaussian | 5 | 3 | 23 | 72 | 0.95 |

# Appendix C

## C-3. Image 2

Image 2 is for Run 1, east-west polarized; there are four 114.3-cm targets in the image. Table C-4 gives correlation values and table C-5 gives number of recognitions.

Table C-4. Image 2 recognition performance: Correlation values.

| Transform method | Target correlation coefficients by dipole orientation | | | | Threshold | No. false alarms |
|---|---|---|---|---|---|---|
| | Vertical | East | West | Horizontal | | |
| FFT | X | 0.698 | 0.784 | 0.845 | 0.60 | 8,020 |
| Gabor | X | 0.822 | 0.889 | 0.894 | 0.66 | 35,748 |
| Haar | 0.663 | 0.728 | 0.810 | 0.812 | 0.60 | 3,973 |
| Gaussian | X | 0.863 | 0.939 | 0.925 | 0.80 | 1,172 |

X = not recognized

Table C-5. Image 2 recognition performance: Number of recognitions.

| Transform method | Target correlation coefficients by dipole orientation | | | | Max false-alarm correlation |
|---|---|---|---|---|---|
| | Vertical | East | West | Horizontal | |
| FFT | X | 14 | 120 | 61 | 0.881 |
| Gabor | X | 40 | 40 | 29 | 0.983 |
| Haar | 4 | 6 | 68 | 49 | 0.864 |
| Gaussian | X | 2 | 56 | 29 | 0.948 |

X = not recognized

## C-4. Image 3

Image 3 is for Run 4, west-west polarized; there is one 114.3-cm target in the image. Table C-6 gives recognition performance

Table C-6. Image 3 recognition performance.

| Transform method | Correlation coefficients for east target | No. of recognitions | No. false alarms | Max false-alarm correlation |
|---|---|---|---|---|
| FFT | 0.620 | 2 | 5,182 | 0.904 |
| Gabor | 0.863 | 30 | 12,068 | 0.979 |
| Haar | X | X | 2,099 | 0.887 |
| Gaussian | 0.925 | 10 | 503 | 0.902 |

X = not recognized

## C-5. Image 4

Image 4 is for Run 6, west-west polarized; there is one 114.3-cm target in the image. Table C-7 gives recognition performance.

Table C-7. Image 4 recognition performance.

| Transform method | Correlation coefficients for east target | No. of recognitions | No. false alarms | Max false-alarm correlation |
|---|---|---|---|---|
| FFT | X | X | 13,019 | 0.915 |
| Gabor | X | X | 29,101 | 0.985 |
| Haar | 0.668 | 2 | 7,054 | 0.898 |
| Gaussian | 0.846 | 10 | 2,601 | 0.957 |

X = not recognized

## C-6. Image 5: 114.3-cm Dipole

Image 5 is for Run 7, west-west polarized. There is one 114.3-cm target and one 166.4-cm target in the image; table C-8 summarizes the recognition performance for the 114.3-cm target.

**Table C-8. Image 5 recognition performance, 114.3-cm dipole.**

| Transform method | Correlation coefficients for east target (114.3 cm) | No. of recognitions | No. false alarms | Max false-alarm correlation |
|---|---|---|---|---|
| FFT | 0.603 | 1 | 2,223 | 0.808 |
| Gabor | 0.735 | 7 | 10,627 | 0.975 |
| Haar | 0.688 | 2 | 1,424 | 0.816 |
| Gaussian | 0.811 | 1 | 387 | 0.953 |

## C-7. Image 5: 166.4-cm Dipole

Table C-9 summarizes the recognition performance for the 166.4-cm target in image 5. (Note: For this case, the thresholds were set to ensure at least one recognition for each transform method.)

**Table C-9. Image 5 recognition performance, 166.4-cm dipole.**

| Transform method | Correlation coefficients for east target (166.4 cm) | No. of recognitions | No. false alarms | Max false-alarm correlation |
|---|---|---|---|---|
| FFT | 0.573 | 2 | 16,280 | 0.842 |
| Gabor | 0.665 | 1 | 53,273 | 0.978 |
| Haar | 0.565 | 1 | 2,072 | 0.777 |
| Gaussian | 0.849 | 1 | 5,265 | 0.978 |

# Distribution

Admnstr
Defns Techl Info Ctr
Attn DTIC-DDA (2 copies)
Cameron Sta Bldg 5
Alexandria VA 22304-6145

Ohio State Univ
Attn R Moses
2015 Neil Ave
Columbus OH 43210-1272

Polytech Univ
Attn L Carin
6 Metrotech Ctr
Brooklyn NY 11201

Univ of Florida Elect Commctn Lab
Attn M Bartlett
PO Box 140245
Gainesville FL 32614-0245

Univ of MD
Ctr for Automtn Rsrch
Attn R Chellappa
AVW Bldg Rm 2365
College Park MD 20742-2375

ARPA/ASTO
Attn T DePersia
3701 N Fairfax Dr
Arlington VA 22203-1714

Army Rsrch Lab
Attn AMSRL-SS-SG M Ressler
Attn AMSRL-D-C Legal Office
Attn AMSRL-OP-SD-TA Mail & Records
  Mgmt
Attn AMSRL-OP-SD-TL Tech Lib
  (3 copies)
Attn AMSRL-OP-SD-TP Tech Pub
Attn AMSRL-SS J Sattler
Attn AMSRL-SS V DeMonte
Attn AMSRL-SS-S J M Miller
Attn AMSRL-SS-SG J McCorkle
Attn AMSRL-SS-SG J Sichina
Attn AMSRL-SS-SG V Sabio (8 copies)

# END
# FILMED

DATE:

9-94

# DTIC